Uniform initial ¹⁰Be/⁹Be inferred from refractory inclusions in CV3, CO3, CR2, and CH/CB chondrites

E.T. Dunham^{1,2,3*}, M. Wadhwa^{1,2}, S.J. Desch², M.-C. Liu³, K. Fukuda⁴, N. Kita⁴, A.T. Hertwig^{3,5}, R.L Hervig², C. Defouilloy⁶, S.B. Simon⁷, J. Davidson^{1,2}, D.L. Schrader^{1,2}, and Y. Fujimoto⁸.

7 8 ¹Arizon

1

2

- ¹Arizona State University (ASU), Center for Meteorite Studies, Tempe, AZ, 85287-1404
- 9 ²Arizona State University, School of Earth and Space Exploration, Tempe, AZ 85287-1404
- ³The University of California, Los Angeles (UCLA), Department of Earth, Planetary and Space
- 11 Sciences, Los Angeles CA 90095-1567.
- ⁴University of Wisconsin-Madison, Department of Geoscience, Madison, WI 53706-1692
- ⁵Universität Heidelberg, Institut für Geowissenschaften, 69120 Heidelberg, Germany
- 14 ⁶CAMECA, 29 quai des Grésillons, 92622 Gennevilliers Cedex, France
- ⁷The University of New Mexico, Institute of Meteoritics, Albuquerque, NM 87131
- 16 ⁸Department of Computer Science and Engineering, University of Aizu, Tsuruga Ikki-machi
- 17 Aizu-Wakamatsu, Fukushima, 965-8580, Japan

18 19

20 21

22

23

24

2526

27

28 29

30

31

32

33 34

35

36

37

38

39

*To whom correspondence should be addressed. E-mail: etdunham@g.ucla.edu.

Abstract

Short-lived radionuclides (SLRs) once present in the solar nebula can be used as probes of the formation environment of our Solar System within the Milky Way Galaxy. The firstformed solids in the Solar System, calcium-, aluminum-rich inclusions (CAIs) in meteorites, record the one-time existence of SLRs such as ¹⁰Be and ²⁶Al in the solar nebula. We measured the ¹⁰Be-¹⁰B isotope systematics in 29 CAIs from several CV3, CO3, CR2, and CH/CB chondrites and show that all except for a FUN CAI record a homogeneous initial ¹⁰Be/⁹Be with a single probability density peak at ${}^{10}\text{Be}/{}^{9}\text{Be} = 7.4 \times 10^{-4}$. Integrating these data with those of previous studies, we find that most CAIs (81%) for which ¹⁰Be–¹⁰B isotope systematics have been determined, record a homogeneous initial ¹⁰Be/⁹Be ratio in the early Solar System with a weighted mean $^{10}\text{Be}/^{9}\text{Be} = (7.1 \pm 0.2) \times 10^{-4}$. This uniform distribution provides evidence that ¹⁰Be was predominantly formed in the parent molecular cloud and inherited by the solar nebula. Possible explanations for why unusual CAIs (FUNs, PLACs, those from CH/CBs, and those irradiated on the parent body) recorded a 10 Be/ 9 Be ratio outside of 7.1 \times 10⁻⁴ include the following: 1) They incorporated a component of ¹⁰Be that was produced in the nebula by irradiation; 2) they formed after normal CAIs; and 3) they were processed (post-formation) in a way that affected their original ¹⁰Be signatures. Given the rarity of these examples, the overall uniformity of initial ¹⁰Be/⁹Be suggests that Solar System ¹⁰Be was predominantly inherited from the molecular cloud.

40 41 42

43

44

45

46

47

48

49

50

1. INTRODUCTION

Calcium-aluminum-rich inclusions (CAIs) are objects that were formed and processed in the early history of the Solar System and recorded conditions in the solar nebula 4.56 Ga ago (MacPherson et al. 1995; Davis and McKeegan 2014). These early-formed solids can be used as probes of local astrophysical conditions during our Sun's formation because they record the evidence of short-lived radionuclides (SLRs) that were present in the early Solar System. Some of these SLRs can even help us to develop a chronology of the events in the solar nebula. Beryllium-10, which decays to 10 B with $t_{1/2} = 1.387$ Ma (Chmeleff et al., 2010; Korschinek et al., 2010), is unique among SLRs because instead of being produced by stars, it is produced

almost exclusively by non-thermal nuclear reactions induced by solar energetic particles (SEPs) and/or galactic cosmic rays (GCRs) (i.e., Davis and McKeegan 2014). To determine the relative contributions from these sources, it is necessary to establish if ¹⁰Be was homogeneously or heterogeneously distributed in the solar nebula soon after the birth of the Solar System. Establishing the origins of ¹⁰Be in turn has implications for the astrophysical environment in which our Solar System formed.

51

52

53

54

55

56

57

58

59 60

61

62

63

64

65

66 67

68 69

70

71

72

73 74

75

76

77

78

79

80

81 82

83 84

85

86

87

88 89

90 91

92

93 94

95

96 97

98

99

100

Prior to the present study, Solar System initial ¹⁰Be/⁹Be ratios were inferred from 38 isochron regressions based on ¹⁰Be-¹⁰B isotopic systematics determined via secondary ion mass spectrometry (SIMS) in CAIs from various chondrites. We count isochron regressions rather than the number of CAIs because some regressions include data from multiple CAIs (for example Gounelle et al. (2013) analyzed 21 CAIs and reported two isochron regressions). It has not been possible to use other Solar System materials to resolve the ¹⁰Be distribution because of its short half-life and the chemical behavior of Be and B that results in low Be/B ratios in most minerals; only CAIs formed early enough and have minerals (i.e., melilite, hibonite, and grossite) with high enough Be/B ratios to determine the initial ¹⁰Be/⁹Be robustly. The ¹⁰Be–¹⁰B isochrons regressed from these data yield initial ¹⁰Be/⁹Be ratios in the range of $(4-100) \times 10^{-4}$ (McKeegan et al., 2000; Sugiura et al., 2001; Marhas et al., 2002; MacPherson et al., 2003; Chaussidon et al., 2006; Liu et al., 2009; Liu et al., 2010; Wielandt et al., 2012; Gounelle et al., 2013; Srinivasan and Chaussidon, 2013; Sossi et al., 2017; Fukuda et al., 2019; Mishra and Marhas, 2019; Fukuda et al., 2021a). Although 25 of these 38 CAI isochron regressions (\sim 66%) have initial 10 Be/ 9 Be consistent with \sim 7 × 10 $^{-4}$ (with 2 sigma uncertainties typically around 30%; Dunham et al., 2020), the data overall have been taken to imply a heterogeneous distribution of ¹⁰Be (Wielandt et al., 2012; Sossi et al., 2017; Fukuda et al., 2019; Fukuda et al., 2021a), which favors a solar nebula irradiation origin. In interpreting the data from these previously studied CAIs, it is noteworthy that most (~80%) of these refractory inclusions are from Vigarano-type carbonaceous (CV) chondrites which typically contain inclusions that are large (> 500 µm) and coarse-grained (i.e., compact type A or type B CAIs); however, these CAIs are not representative of the whole chondrite CAI population (i.e., MacPherson 2014). The CV3 chondrites can be categorized as CV3_{oxidized (ox)} or CV3_{reduced (red)} based on the type of alteration they have experienced. Those that are oxidized (i.e., CV3_{ox}) are known to have experienced a greater degree of aqueous alteration and thermal metamorphism (Krot et al., 1998). These effects may not influence the initial ¹⁰Be/⁹Be ratios inferred in CV CAIs, but it would nonetheless be useful to ascertain if CV CAIs record a similar range of initial ¹⁰Be/⁹Be as CAIs from other types of carbonaceous chondrites. Chondrites which are thought to be less altered (by aqueous alteration or thermal metamorphism) include the Ornanstype carbonaceous (CO) and Renazzo-type carbonaceous (CR) chondrites because they contain higher abundances of presolar materials and less petrographic evidence of thermal metamorphism, respectively (Davidson et al., 2019a, b; Simon et al., 2019b; Schrader et al., 2011, 2015; Simon and Grossman, 2015). The High-iron/Bencubbin-type carbonaceous (CH/CB) chondrite Isheyevo may have experienced mild thermal metamorphism, but appears to have largely escaped post-accretionary aqueous alteration (Krot et al., 2008).

In addition to normal CAIs from different carbonaceous chondrites, CAIs that are isotopically distinct have also been studied previously for 10 Be $^{-10}$ B isotope systematics. When compared to normal CAIs, FUN (fractionated and unidentified nuclear effects) CAIs and PLACs (platy hibonite crystals) typically have lower inferred 26 Al/ 27 Al ratios and have large nucleosynthetic isotopic anomalies in elements such as Ca, Ti, Cr, Sr, Ba, Nd, and Sm (Krot et al., 2014; Kööp et al., 2016; Park et al., 2017; Kööp et al. 2018). The FUN CAIs are mineralogically similar to normal CAIs, but have experienced a high degree of evaporation, as evidenced by large mass-dependent fractionation effects in elements such as O, Mg, and Si. PLACs are composed of hibonite, and have up to 2 orders of magnitude larger nucleosynthetic

anomalies than FUN CAIs; about 80% of PLACs and related objects have significant mass fractionation effects (Kööp et al. 2016). These traits have been suggested to indicate that FUN CAIs and PLACs formed before the introduction of ²⁶Al into the early Solar System (Park et al., 2017; Krot et al., 2014). However, it is also possible that either they reflect ²⁶Al heterogeneity in the early solar nebula or perhaps they formed late or experienced reequilibration after the decay of ²⁶Al, after most other CAIs in a solar nebula with a homogeneous, canonical ²⁶Al abundance. Previous studies have found that FUN CAIs and PLACs recorded ¹⁰Be/⁹Be ~(3–5) × 10⁻⁴, lower than most regular CAIs (Liu and Keller, 2017; Wielandt et al., 2012; MacPherson et al., 2003). Due to their many other distinctive qualities, it may not be surprising that FUN CAIs and PLACs are distinct from normal CAIs with respect to their ¹⁰Be abundance; however, the reason for these differences is not yet clear.

The distribution of ¹⁰Be in CAIs is key for determining the origin of ¹⁰Be. If all CAIs record the same initial ¹⁰Be/⁹Be ratio, then ¹⁰Be can be inferred to be homogeneously distributed in the CAI-forming region in the early Solar System, while if CAIs display a range of initial ¹⁰Be/⁹Be values, then ¹⁰Be was heterogeneous at the time of CAI formation. A homogeneous early Solar System ¹⁰Be distribution could provide evidence that ¹⁰Be formed by galactic cosmic ray (GCR) spallation, likely in the molecular cloud (Desch et al., 2004), where energetic (> tens of MeV) protons and alpha particles interacted with molecular cloud C, N and O nuclei to efficiently produce ¹⁰Be. The penetration depth of GCRs exceeds 100 g/cm², much greater than the column density of molecular clouds, so they irradiate the cloud uniformly (Desch et al., 2004). This process would have continued until the molecular cloud collapsed to form our solar nebula. On the other hand, a heterogeneous ¹⁰Be distribution in the early Solar System would be evidence that ¹⁰Be was largely produced by solar cosmic ray spallation of nebular C, N, and O gas and/or solids (Gounelle et al., 2001; MacPherson et al., 2003; Gounelle et al., 2006; Liu et al., 2010; Wielandt et al., 2012; Sossi et al., 2017; Fukuda et al., 2021a). In this scenario, 10 Be production would be a function of both heliocentric distance r from the Sun (with greater production closer to the Sun) and time t from the beginning of the Solar System (when $t \sim 0$), due to the changing solar activity of the young Sun and the evolution of the protoplanetary disk (Jacquet, 2019). To the extent that CAIs formed at different times and/or places, this process would result in a non-uniform distribution of ¹⁰Be in CAIs. However, if all CAIs formed at essentially the same time (i.e., t < 0.1 Ma) and heliocentric distance (r < 0.1 AU) in the solar nebula, the ¹⁰Be distribution in CAIs is be predicted to be the same for both the molecular cloud inheritance model and the irradiation in the disk model.

We note that recent studies do not provide a consensus on the precise location and duration of CAI formation and high-temperature processing. CAI relative chronometry suggests that these objects were formed and were thermally processed over timespans ranging from ~40,000 years to ~200,000 years (Connelly et al., 2012; MacPherson et al., 2012; Kita et al., 2013; Mishra and Chaussidon, 2014; Liu et al., 2019; Kawasaki et al., 2019). It is theoretically possible that high-temperature processing of CAIs could have lasted as long as ~1 Ma because temperatures in the disk are predicted to exceed ~1300 K for this extended time interval (Yang and Ciesla, 2012). Moreover, some CAI isotopic compositions suggest that these solids formed over a wide spatial range in the early Solar System (Brennecka et al., 2020). Although it is difficult to predict exactly when and where CAIs formed, the data and models together strongly suggest that all CAIs did not form at the same time or place, and variable ¹⁰Be/⁹Be is likely be expected in an irradiation model.

We combine the predictive models of Yang and Ciesla (2012) and Jacquet (2019) to estimate 10 Be distribution in CAIs to assess the degree of expected 10 Be heterogeneity in the irradiation model. Jacquet (2019) predicts that the 10 Be abundance would decrease with r (i.e., distance from the Sun in AU), and increase with time t, for both irradiation of gas and solids, so that the 10 Be/ 9 Be recorded by a CAI would scale as r $^{-3/2}$ t $^{+1}$. Depending on the disk model

and where and when CAIs form, they could record a great range in values, possibly spanning an order of magnitude, especially as the r where CAIs can form shrinks over time. Even in an initially expanding disk model like that of Yang and Ciesla (2012), where r initially increases with time, a significant fraction of CAIs is expected to differ from the mean in terms of initial ¹⁰Be abundance. Specifically, Yang and Ciesla (2012) found that temperatures in an evolving disk exceed ~1300 K (i.e., conditions under which CAIs could form or undergo thermal processing) for $r < r_{1300}(t) \approx 1.4 (t/0.3 \text{ Ma})^{0.63} \text{ AU}$ for t < 0.3 Ma, and $t < r_{1300}(t) \approx 1.4 (t/0.3 \text{ Ma})^{0.63}$ Ma)⁻¹ AU for t > 0.3 Ma. Assuming CAIs formed between 0.5 AU and $r_{1300}(t)$ they would be expected to record ¹⁰Be/⁹Be values that varied by at least a factor of 2. Specifically, if the mean of all CAIs was 10 Be/ 9 Be $\sim 7 \times 10^{-4}$, as suggested by CAI data, those formed or thermally processed by t = 0.3 Ma are predicted to record values between 3 and 13×10^{-4} , and those formed or processed after t = 0.3 Ma would record values between 6 and 21×10^{-4} . It is also predicted that >50% of CAIs would have ${}^{10}\text{Be}/{}^{9}\text{Be} < 5 \times 10^{-4} \text{ or} > 10 \times 10^{-4}$, resolvably different from a mean value of $\sim 7 \times 10^{-4}$. Although this is our estimate for the particular model of Yang and Ciesla (2012), the spread in ¹⁰Be/⁹Be values is predicted to increase for models in which most CAIs formed while $r_{1300}(t)$ was decreasing in time, and a greater fraction of CAIs would be inconsistent with 10 Be/ 9 Be $\sim 7 \times 10^{-4}$. It would seem to be a robust prediction of irradiation models that a large fraction (>~50%) of CAIs would record ¹⁰Be/⁹Be values significantly different than in most CAIs. Therefore, if more than 50% of CAIs actually record ¹⁰Be/⁹Be values consistent with the mean, inheritance from the molecular cloud likely contributed significantly to the ¹⁰Be inventory of the solar nebula. A hybrid model has been suggested in which enough 10 Be was inherited to produce 10 Be/ 9 Be $\sim 4 \times 10^{-4}$, with irradiation in the nebula contributing the remainder to result in a mean 10 Be/ 9 Be $\sim 7 \times 10^{-4}$ (Wielandt et al., 2012). Such a scenario invokes half the irradiation-produced ¹⁰Be compared to the end-member scenario (Jacquet, 2019). Even in this scenario, a significant fraction (likely > 25%) of CAIs would have 10 Be/ 9 Be ratios greater than $\sim 7 \times 10^{-4}$. Although these fractions are approximate estimates, they allow us to evaluate CAI data in the context of the irradiation in the solar nebula versus molecular cloud inheritance models.

In this study, our goal is to understand the origin of ¹⁰Be in the early Solar System by better constraining the distribution of ¹⁰Be in CAIs as well as the fraction of CAIs that record a single ¹⁰Be/⁹Be value. As such, we have determined the ¹⁰Be-¹⁰B isotope systematics in a diverse set of 29 CAIs from CV3.1–3.6 (n=11), CO3.00–3.3 (n=8), CR2–2.7 (n=5), and CH/CB (n=5) chondrites and infer the initial ¹⁰Be/⁹Be ratios in these inclusions (we note that the subtypes of some of these chondrites have not yet been determined). In addition to normal CAIs, our sample set includes a FUN CAI, an UN CAI, and a forsterite-bearing type B (FoB) CAI. We have integrated our data with previously reported ¹⁰Be-¹⁰B results from the literature, increasing the total number of CAI ¹⁰Be-¹⁰B isotope regressions reported from 38 to 63. For a subset of these CAIs, we also assessed whether the inferred initial ¹⁰Be/⁹Be ratios are correlated with ²⁶Al/²⁷Al ratios, oxygen isotopic compositions, excesses of ⁵⁰Ti, and rare earth element (REE) abundances, because such relationships can potentially provide insights into their formation, alteration, and metamorphic histories.

2. METHODS

2.1. Samples and electron probe microanalysis (EPMA)

Meteorites were obtained for this study from the ASU Buseck Center for Meteorite Studies collection, the ANSMET collection, and collaborators. Some of the CAIs studied here (Isheyevo CAIs, Northwest Africa (NWA) 5028 CAIs, Dar al Gani (DaG) 027 CAIs *Goeppert* and *Jemison*, and DaG 005 CAI *Mitchell*) were located by elementally mapping meteorite

sections obtained using the JEOL JXA-8530F electron probe microanalyzer (EPMA) in the Eyring Materials Center at ASU. The elemental maps for Miller Range (MIL) 090657 were from Davidson et al. (2019b). After the CAIs were found or obtained, polished sections containing identified CAIs were characterized using ASU's EPMA; elemental maps, backscattered electron (BSE) and secondary electron (SE) images were obtained, along with mineral compositions using electron dispersive and wavelength dispersive spectroscopy (EDS and WDS). The analytical conditions included a 20 kV, 20 nA electron beam, and the standards used for ZAF corrections included San Carlos augite, Hakone anorthite, orthoclase, Kakanui hornblende, rutile, Johnstown hypersthene, chromite, and Durango apatite. Images of the CAIs are shown in Fig. 1; Table 1 provides descriptions of each inclusion. Representative chemical compositions of phases in these CAIs are shown in Table 2. The location and quality of the SIMS analysis craters were checked with ASU's EPMA after isotopic analysis. Although the CAIs from the four distinct chondrite groups studied here (CV3, CO3, CR2, and CH/CB) vary in size, abundance, mineralogy, texture, and shape, they are generally melilite-rich \pm spinel \pm perovskite \pm hibonite \pm grossite \pm pyroxene \pm anorthite and show little or no evidence for the presence of alteration minerals (such as phyllosilicates, calcite, and sodalite). While we selected samples showing minimal alteration, we also made an effort to avoid analyzing any phases except for the early-formed ones in the CAIs.

Table 1 Characteristics of the CAIs studied here.

201

202203

204

205206

207

208

209

210

211

212

213

214215

216217

218

219220

221

Chondrite type	Meteorite name	CAI name	Longest dimension	Åk range	Other CAI characteristics
CV3 _{ox}	NWA 6991	B4	10 mm	15–36	CTA, predominately composed of coarse melilite grains, along with pyroxene, spinel, and minor anorthite; secondary alteration is only a minor component.
CV3 _{ox}	Allende	CMS-1	5 mm	35–41	FUN Type B, irregularly shaped igneous inclusion composed mainly of pyroxene and melilite grains poikilitically enclosing abundant spinel and distinct generations of melilite.
CV3 _{ox}	Allende	TS23A	10 mm	22–76	Type B1, rounded shape with monomineralic melilite mantle surrounding a core with melilite laths, blocky pyroxene, and interstitial anorthite as well as ubiquitous spinel.
CV3 _{ox}	Allende	TS68	5 mm	10–40	CTA, rounded shape, contains large (up to 700 µm) stubby melilite crystals and coarse pyroxene, euhedral spinel is heterogeneously distributed in the sample, lightly altered and contains fremdlinge (FeNimetal, Pt-metal alloys, V-rich magnetite, sulfides, and phosphates).
CV3 _{ox} *	NWA 7891	ZT4	5.2 mm	12	CTA or FTA, irregular rounded shape with distinct embayments, consists predominately of porous melilite, margins are perovskite-rich, surrounded by a spinel-pyroxene rim.

CV3 _{ox}	NWA 3118	ZT7	3.3 mm	21–24	CTA, rounded partially rimmed fragment consisting of predominately melilite enclosing spinel occurring as chains and as isolated grains, interstitial perovskite, some alteration near the rim.
CV3 _{red} *	NWA 5028	Agave	5 mm	6–39	Type B2, dominated by pyroxene, which encloses patches of melilite and anhedral spinel; only minimal alteration products are present.
CV3 _{red} *	NWA 5028	Cholla	1 mm	7–39	FTA, contains anhedral spinel, typically 10 μm diameter, enclosed in melilite, inclusion surrounded by an irregular ~40 μm thick pyroxene rim. Extended spinel-pyroxene inclusions around the main inclusion. The only alteration found in the CAI is a patch of secondary anorthite.
CV3 _{red} *	NWA 5508	Saguaro	18 mm	9–35	Type B2, composed predominately of melilite, with pyroxene, spinel, and anorthite. Spinel is often distributed as rounded palisade bodies surrounding melilite, pyroxene, and spinel. Includes minimal alteration products.
CV3_{red}	Vigarano	FoB 3137	6 mm	71–87	FoB, rounded shape with nodular segments, outer zones which are forsterite-free but melilite-rich and an interior forsterite region enclosed in pyroxene and melilite.
CV3_{red}	Leoville	ZTI	6.3 mm	31	Type B, irregular and fragmented shape, mantle is predominantly melilite and core is composed of melilite enclosing sections of pyroxene and anorthite, spinel dispersed throughout and tends to clump in palisade bodies, partial rim.
CO3	DOM 08006	31-2	220 μm	2–44	Hibonite- and grossite-rich, irregular shape, concentric layers of hibonite, grossite, melilite, pyroxene, forsterite, and enstatite from core to rim.
CO3	DaG 027	Anning	830 μm	8–13	CTA-like, rounded shape, some coarse melilite, most melilite encloses spinel, hibonite, and perovskite.
CO3	DaG 005	Bascom	720 μm	9–18	CTA-like, irregular shape, melilite nodules enclosing spinel clumps, minimal alteration in cracks.
CO3	DaG 027	Goeppert	340 μm	7–10	CTA-like, fragmented, elongate, rounded shape, melilite surrounding spinel clumps, faulted partial pyroxene rim.
CO3	DaG 027	Jemison	300 μm	12–15	CTA-like, fragmented, rounded shape, melilite enclosing rounded spinel, partial pyroxene rim.
CO3	DaG 027	Krafft	640 μm	22–34	CTA-like, somewhat rounded shape, melilite-rich with spinel clumps.

CO3	NWA 7892	Mesquite	5 mm	5	CTA-like, rounded shape, interior composed of melilite with hibonite (and minor calcite), mantle composed of hibonite and spinel, complete multi-mineralic rim composed of melilite, spinel, and hibonite.
CO3	DaG 005	Mitchell	370 μm	5–6	CTA-like, irregular shape, melilite-rich with concentrations of spinel, hibonite, and perovskite in the interior, thin partial pyroxene rim.
CR2	NWA 801	Cereus	900 μm	10–14	CTA-like, rounded porous CAI consisting of melilite enclosing small rounded spinel grains and minimal anorthite (concentrated near the rim of the inclusion), complete rim is a thin layer of clustered spinel grains and a ~10 µm thick layer of pyroxene, no secondary mineralization.
CR2	MIL 090657	Creosote	900 μm	16–32	CTA-like, rounded fragment dominated by melilite enclosing chains of small round spinel grains, and patches of small anorthite and pyroxene (TiO ₂ up to 18%) grains, partial rim (composed of sequential layers of spinel, anorthite, and pyroxene) that occasionally curves into the CAI interior, minimal presence of a Caalteration mineral.
CR2	Shişr 033	Dalea	220 μm	12–37	Type A-like, rounded porous CAI composed of melilite enclosing small intermixed euhedral anorthite and spinel grains, thick pyroxene rim, an Fe-oxide vein passes through the edge.
CR2	NWA 801	Palo Verde	250 μm	18–23	CAI fragment consisting of melilite and calcite; irregularly shaped melilite grain rimmed with secondary calcite.
CR2	MIL 090657	Yucca	950 μm	23–30	CTA-like, rounded fragment composed of melilite enclosing pyroxene (TiO ₂ of 11–13 wt.%) and large euhedral spinel grains, surrounded by a partial rim (consisting of sequential layers of spinel, anorthite, and pyroxene), no secondary alteration. Could potentially be a fragment of a Type B1-like inclusion.
СН/СВ	Isheyevo	Bell	120 μm	5–17	Melilite-rich rounded inclusion fragment with abundant lath- shaped grossite grains, few lath-shaped spinel occur along the edge.
СН/СВ	Isheyevo	Meitner	180 μm	5–17	Melilite-rich rounded inclusion fragment, melilite encloses grains of rounded spinel and perovskite, partial pyroxene rim.
CH/CB	Isheyevo	Rubin	150 μm	5–17	Melilite-rich inclusion fragment, melilite encloses spinel and one edge is rimmed by pyroxene.

CH/CB	Isheyevo	Tereshkova	290 μm	5–17	Melilite-rich rounded inclusion with abundant hibonite grains and some interspersed perovskite.
CH/CB	Isheyevo	Tharp	180 μm	5–17	Melilite-rich rounded inclusion fragment, spinel and perovskite dispersed heterogeneously, and a partial rim.

^{*}We re-classified or sub-classified these chondrites, see Supplementary Materials. 222

228 Table 2

227

229 Representative mineralogy and chemical composition (in wt.%) of the CAIs studied here.

Meteorite name	CAI	Mineral	Al_2O_3	Na ₂ O	TiO ₂	CaO	SiO ₂	MgO	Cr ₂ O ₃	FeO	Sum	Åk
CV3 _{ox} NWA 6991	B4	px	19.05	bdl	12.74	25.31	34.43	7.85	bdl	bdl	99.37	
		mel	28.13	bdl	0.04	42.00	26.21	3.35	bdl	0.08	99.80	21
CV3 _{ox} Allende	CMS-1	px	19.55	bdl	9.08	25.16	37.38	8.94	bdl	bdl	100.10	
		mel	22.78	0.08	0.05	41.09	30.33	5.63	bdl	bdl	99.96	40
		mel	26.02	bdl	0.04	40.95	28.77	4.41	bdl	bdl	100.20	29
CV3 _{ox} * NWA 7891	ZT4	sp	70.63	bdl	0.17	0.14	bdl	27.58	0.13	1.05	99.66	
		sp	70.6	bdl	0.19	0.11	bdl	27.61	0.14	1.27	100.01	
		mel	34.79	bdl	0.04	41.75	22.53	0.71	bdl	bdl	99.80	4
		mel	31.59	bdl	bdl	41.45	24.37	1.92	bdl	bdl	99.37	11
		pv	0.95	bdl	56.89	41.01	0.32	bdl	0.05	0.06	99.31	
		px	3.67	bdl	0.25	25.29	52.74	18.24	0.05	0.24	100.48	
CV3 _{ox} NWA 3118	ZT7	mel	23.89	0.25	0.20	41.39	28.7	5.12	bdl	bdl	99.55	35
CV3 _{red} NWA 5028	Agave	mel	36.28	bdl	bdl	41.02	21.41	0.20	bdl	0.07	99.04	1
	C	px	14.79	bdl	4.64	25.2	42.75	12.27	bdl	0.11	99.81	
		px	8.48	bdl	1.28	25.41	48.37	15.44	0.05	0.06	99.10	
		px	13.42	bdl	1.97	25.37	45.19	13.31	0.04	0.07	99.40	
		sp	71.35	bdl	0.06	0.16	0.08	27.96	0.93	0.15	100.69	
		hib	85.44	bdl	4.29	8.52	0.35	2.29	0.04	bdl	101.00	
CV3 _{red} NWA 5028	Cholla	mel	30.46	bdl	0.08	41.61	24.65	2.60	bdl	bdl	99.43	16
CV Jred IVVIA 3020	Chona	mel	35.50	bdl	0.03	41.62	21.51	0.64	bdl	bdl	99.30	4
		px	20.67	bdl	11.66	25.17	33.81	7.86	bdl	0.20	99.30	7
CV3 _{red} * NWA 5508	Saguaro	mel	33.29	bdl	0.08	41.44	23.22	1.53	bdl	bdl	99.49	10
CVJred IVWA JJ00	Saguaro	mel	25.86	bdl	bdl	41.81	28.13	4.17	bdl	bdl	99.98	28
CV3 _{red} Leoville	ZT1		19.56	bdl	7.97	24.69	38.57	8.76	bdl	bdl	99.66	20
C V 3red LCOVIIIC	211	px mel	23.85	bdl	bdl	41.62	29.35	4.81	bdl	bdl	99.69	34
		mel	11.14	0.21	bdl	41.58	37.81	10.00	bdl	bdl	100.85	69
		an	35.20	0.21	0.07	18.90	42.88	0.29	bdl	1.74	99.17	09
CV3 _{red} Vigarano	3137	mel	4.63	0.08	bdl	41.40	41.83	12.41	bdl	0.07	100.52	87
C V 3red V Igarano	3137	mel	17.07	0.19	bdl	41.41	34.11	7.44	bdl	bdl	100.32	53
CO3 DaG 027	Anning	mel	32.30	bdl	0.06	41.41	24.25	1.41	bdl	0.12	99.46	8
CO3 DaG 027	Anning		69.88	bdl	0.06	0.12	bdl	27.42	0.12	1.83	99.40	0
		sp hib	86.03	bdl	3.22	8.56	0.18	1.81	bdl	0.29	100.21	
CO3 DaG 005	Bascom	mel	30.58	bdl	bdl	41.31	25.36	2.13	bdl	0.29	99.56	13
CO3 DaG 003	Dascoili	mel	33.30	bdl	0.05	41.52	23.58	1.06	bdl	0.14	100.02	6
CO3 DaG 027	Goeppert	mel	32.18	bdl	bdl	41.93	24.02	1.54	bdl	0.46	99.91	9
CO3 DaG 027	Goeppert		33.21	bdl	0.04	42.00	23.12	1.07	bdl	0.23	99.91	6
CO3 DaG 027	Jemison	mel mel	30.97	bdl	0.04	41.62	24.97	2.08	bdl	0.31	99.8 99.91	13
CO3 DaG 027	Jennson	mel	33.98	bdl	bdl	41.59	23.13	0.88	bdl	0.22	99.76	5
		mel	31.87	bdl	bdl	41.64	24.60	1.65	bdl	0.13	100.02	10
								0.74		0.20	100.02	4
CO3 DaG 027	Krafft	mel	34.27	bdl	0.04	41.87	23.14	3.94	bdl		99.61	
CO3 DaG 027	Kiaiii	mel	25.83	bdl	bdl 0.06	41.27	28.45		bdl	bdl	99.01	26 3
		mel	35.01	bdl	0.06	41.48	22.79	0.48	bdl 0.12	0.11		3
CO2 D. C.005	NC(1 11	sp	70.48	bdl	0.41	0.07	bdl	28.61	0.12	0.24	99.88	
CO3 DaG 005	Mitchell	mel	35.43	bdl	0.09	42.02	22.18	0.25	bdl	0.25	100.26	1
		mel	35.67	bdl	0.16	42.05	21.97	0.11	bdl	0.18	100.14	1
		mel	35.59	bdl	0.22	42.26	21.83	0.10	bdl	0.20	100.22	1
CO2 DOM 00006	21.2	mel	34.62	bdl	0.07	41.64	22.59	0.42	bdl	0.29	99.66	2
CO3 DOM 08006	31-2	grs	77.87	bdl	0.09	21.58	bdl 25.04	0.07	bdl	0.25	99.84	10
CR2 LAP 02342	Cereus	mel	30.93	bdl	0.19	41.66	25.04	1.99	bdl	bdl	99.81	12
CDA MY COCCE		mel	33.71	bdl	0.08	41.80	23.24	1.03	bdl	0.10	99.96	6
CR2 MIL 090657	Creosote	mel	26.08	bdl	bdl	40.18	28.66	4.38	0.05	0.22	99.58	31
		mel	29.41	bdl	bdl	40.69	25.33	2.72	bdl	bdl	98.24	18
		an	36.69	0.04	0.05	21.17	41.84	0.14	bdl	bdl	99.97	

FTA = fluffy type A223

CTA = compact type A224

²²⁵

FoB = forsterite-bearing type B
FUN = Fractionation and Unknown Nuclear 226

		an-rim hibonite	36.81 82.93	bdl bdl	0.02 6.45	21.15 8.40	41.87 bdl	0.26 3.31	bdl 0.08	0.16 bdl	100.34 101.16	
		px	24.19	bdl	18.42	24.57	27.49	4.36	0.05	bdl	99.12	
		px-rim	3.41	bdl	0.44	25.53	51.85	16.54	0.05	0.29	98.13	
CR2 Shişr 033	Dalea	mel	33.89	bdl	bdl	40.73	23.68	1.37	bdl	0.17	99.82	8
Crc2 omgr 055	Buica	mel	29.42	bdl	bdl	40.9	26.13	2.93	bdl	0.25	99.63	20
		px	1.27	bdl	0.08	25.41	54.46	18.57	bdl	0.30	100.10	20
		sp	69.44	bdl	0.16	0.39	0.33	27.77	0.27	0.36	98.70	
		an	37.01	bdl	0.05	20.29	42.49	0.15	bdl	0.26	100.25	
CR2 NWA 801	Palo Verde	mel	27.48	bdl	bdl	41.25	27.09	3.22	bdl	0.74	99.78	21
		mel	26.57	bdl	0.12	40.73	27.94	3.43	bdl	1.03	99.82	23
CR2 MIL 090657	Yucca	mel	28.54	bdl	bdl	40.30	27.34	3.57	bdl	0.16	99.89	21
		mel	27.32	bdl	bdl	40.35	27.67	3.92	bdl	bdl	99.37	26
		px	20.05	bdl	6.61	24.70	38.95	9.08	0.04	bdl	99.48	
		px-rim	1.49	bdl	0.10	22.87	52.61	17.75	0.31	1.66	96.98	
		sp	70.38	bdl	0.43	0.09	0.39	28.10	0.18	0.31	99.88	
		an-rim	27.12	0.05	0.23	20.73	44.04	5.11	0.16	1.85	99.32	
Isheyevo	Burnell	mel	36.12	bdl	0.04	40.72	22.49	0.25	bdl	0.12	99.79	1
		mel	35.10	bdl	0.04	40.46	23.43	0.43	bdl	0.23	99.69	2
		grs	69.35	bdl	0.31	24.40	3.98	0.20	bdl	1.09	99.28	
	Meitner	mel	36.48	bdl	0.12	40.42	22.46	0.36	bdl	0.15	99.98	2
		mel	34.36	bdl	0.07	40.66	23.76	1.07	bdl	0.30	100.27	6
	Rubin	mel	31.01	bdl	bdl	40.70	26.00	2.40	bdl	0.55	100.74	14
		mel	30.67	bdl	bdl	40.93	26.42	2.71	bdl	0.62	101.37	16
	Tereshkova	mel	33.54	bdl	0.12	39.73	22.40	0.78	bdl	0.40	96.99	5
		mel	33.93	bdl	0.11	40.27	22.21	0.44	bdl	0.13	97.09	3
		hib	85.12	bdl	1.61	8.51	bdl	0.79	bdl	0.16	96.15	
	Tharp	mel	32.83	bdl	0.04	41.37	23.90	1.33	bdl	0.38	99.86	8
		mel	30.35	bdl	bdl	41.13	25.34	2.24	bdl	0.31	99.45	14

*We re-classified or sub-classified these chondrites, see Supplementary Materials.

231 Detection limits are: K₂O 0.02 wt.%, CaO 0.02 wt.%, Al₂O₃ 0.02 wt.%, SiO₂ 0.03 wt.%, Na₂O

232 0.03 wt.%, MgO 0.02 wt.%, TiO₂ 0.03 wt.%, Cr₂O₃ 0.03 wt.%, FeO 0.06 wt.%.

mel = melilite, sp = spinel, px = pyroxene (ranging from Al- Ti-rich pyroxene to diopside), an = anorthite, grs = grossite, hib = hibonite, pv = perovskite, bdl = below detection limit. K₂O was measured but was below the detection limit in all analyses.

Mineralogy information for CAIs *Mesquite*, *TS23* and *TS68* can be found in (Hertwig et al., 2021; Simon et al., 1994, 1999)

Åk = 100*Mg/(Mg+Al/2) (mol.%)

239 240 **2.2. SIMS** ¹⁰Be-¹⁰B Analyses

238

241242

243

244

245

246

247

248249

250

251

252

253254

255

256

257

258

259

The ¹⁰Be–¹⁰B isotope systematics in 29 CAIs were determined using the Cameca IMS-6f SIMS at ASU (for most CV3 CAIs studied here) and the Cameca IMS-1290 SIMS at UCLA (for most CR2, CO3, and CH/CB CAIs studied here). Because the analyses took place over many sessions, the conditions are varied and are detailed in the Supplementary Materials. We analyzed melilite in all CAIs except one (grossite was measured in CAI 31-2) with a primary $^{16}\text{O}^-$ or $^{16}\text{O}_3^-$ beam current of 10–25 nA resulting in a spot size $\Phi \sim 10-30$ um, and we measured secondary ions ¹⁰B⁺, ¹¹B⁺, and ⁹Be⁺ (to determine ¹⁰B/¹¹B ratios and to calculate Be and B concentrations for determining Be/B ratios). Up to 15 minutes of pre-sputtering was necessary to remove surface boron contamination; we monitored the B signal as it dropped to a stable value, signaling that the surface B was removed. We operated the mass spectrometer at a mass resolving power (MRP) $M/\Delta M > 1200$, sufficient to resolve and avoid hydride (especially $^9\mathrm{BeH^+}$) and $\mathrm{Al^{3+}}$ interferences. Although M/ Δ M \sim 1400 will completely resolve $^9\mathrm{BeH^+}$, due to the low counts, we were able to avoid the signal on the shoulder of the ¹⁰B peak from ⁹BeH⁺ at a mass resolution power of ~1200 on the IMS-6f. NIST 610, NIST 614, melilite-composition glasses (Dunham et al., 2020), and IMt-1 illite clay were used as standards to characterize the relative sensitivity factor (RSF) and instrumental mass fractionation (IMF) using the equations below. The RSF ranged from \sim 2.0 to \sim 3.5 and the IMF from \sim 1.03 to \sim 1.07 depending on the session and instrument (monocollection IMS-6f versus multi-collection IMS-1290). The

background signals of the electron multipliers (EMs) on the multi-collection 1290 were ~0.003 cps. Subtracting this background from the Be and B counts does not change the measured isotopic composition, considering the uncertainties. Uncertainties for the corrected isotope ratios were calculated by adding in quadrature uncertainties from counting statistics and uncertainties associated with measurements of the standards. Resulting data are shown in Table 3. The RSF affecting the Be/B ratio is defined as:

$$RSF = \left(\frac{{}^{9}Be^{+}}{{}^{11}B^{+}}\right)_{SIMS} / \left(\frac{{}^{9}Be}{{}^{11}B}\right)_{true},$$

where (${}^{9}\text{Be}^{+/11}\text{B}^{+}$)_{SIMS} is the ${}^{9}\text{Be}/{}^{11}\text{B}$ ion ratio measured via SIMS and (${}^{9}\text{Be}/{}^{11}\text{B}$)_{true} is the true atomic ${}^{9}\text{Be}/{}^{11}\text{B}$ ratio in a reference material. It has been determined that the RSF does not change significantly if standards have a different composition than the unknown material (Dunham et al., 2020; Fukuda et al., 2018). The IMF affecting the ${}^{10}\text{B}/{}^{11}\text{B}$ ratio is defined as:

274 IMF =
$$\left(\frac{^{10}B^{+}}{^{11}B^{+}}\right)_{SIMS} / \left(\frac{^{10}B}{^{11}B}\right)_{true}$$
.

IMS-1290 (UCLA) measurements of ¹⁰Be-¹⁰B systematics

We used three distinct calibration techniques for the CAIs analyzed via this instrument. In all cases, we generated the primary ion beam with the *Hyperion-II* source.

1. Mono-collection spot analysis

We analyzed CAI *CMS-1* with a primary $^{16}O^{-}$ beam current of 10–15 nA resulting in a beam size $\sim 5 \times 4 \ \mu m^2$; the mass resolving power (MRP) was ~ 2000 , and ^{9}Be (10s), ^{10}B (20s), ^{11}B (15s), and $^{28}Si^{++}$ (3s) were counted for 10–50 cycles depending on the B count rates. NIST 614 was used as the running standard through the session for RSF and IMF corrections, and to check for instrumental drift throughout the day; NIST 610, with higher concentrations of Be and B, was measured at the beginning and end of session days.

2. Multi-collection spot analysis

We analyzed CAI *CMS-1* again, as well as a suite of CR2 and CO3 CAIs in this mode. The primary ¹⁶O⁻ beam current of 10 nA resulted in a beam size ~5 × 4 µm². Secondary ion intensities were measured under mass resolving power of ~2500 in dynamic multi-collection mode. In this setting, we first collected ²⁷Al⁺⁺⁺ and ²⁸Si⁺⁺⁺ simultaneously for 5 seconds, then ⁹Be for 10 seconds after one mass jump, and then ¹⁰B and ¹¹B for 30 seconds as the last step. The NIST 614 glass standard was measured throughout the analysis session, and NIST 610 as well as melilite composition glasses were measured at the beginning of the session or when conditions changed, to obtain the RSF for determining ⁹Be/¹¹B, and to correct for the IMF to determine the ¹⁰B/¹¹B ratio. Melilite-composition glasses with a range of Be/B ratios were measured at the beginning of the session to verify that there were no resolvable matrix effects on the RSF.

3. Multi-collection using O₃⁻ raster analysis

We analyzed another suite of CO3 CAIs as well as CH/CB CAIs and a Forsterite-bearing type B (FoB) CAI in this mode. A primary beam of $^{16}\text{O}_3^-$ at 1–2 nA was initially rastered over a $10 \times 10~\mu\text{m}^2$ area during the "pre-sputtering" period (to remove terrestrial boron contamination on the surface). During the analysis, the primary beam raster was reduced to 5 \times 5 μm^2 . Secondary ion intensities were measured with multiple EMs with a mass resolving power of ~2500 in dynamic multi-collection mode (first collected $^{27}\text{Al}^{++}$ and $^{28}\text{Si}^{++}$

simultaneously for 5 seconds, then ⁹Be for 10 seconds after one mass jump, and then ¹⁰B and ¹¹B for 30 seconds as the last step). NIST 610, 614, and melilite-glass standards were used to determine the RSF and IMF correction factors.

For CAI *CMS-1*, in compiling data from 3 separate SIMS sessions, we found spots with ${}^9\mathrm{Be/}{}^{11}\mathrm{B}$ up to 80 via the IMS-1290, but our measurement uncertainties are large for these analyses (2SE errors on the ${}^9\mathrm{Be/}{}^{11}\mathrm{B}$ ratio in the range of 1–9%) because there were only ~20 usable cycles per analysis; the primary beam sputtered into phases other than melilite (usually spinel) in some analyses, revealed by an increase in the boron ion intensity and a change in the boron isotope ratio. Thus, only a few measurement cycles could be used in such analyses, resulting in lower precision.

Comparing ¹⁰Be–¹⁰B analytical configurations and instruments

As described above, we used two SIMS instruments (IMS-6f and IMS-1290) and 4 separate analytical conditions to measure the ¹⁰Be–¹⁰B isotope systematics in 29 CAIs. The smallest IMS-6f SIMS beam spot diameter that was feasible for our IMS-6f analyses was ~20 μm. However, melilite grains in CAIs from CO3, CR2, and CH/CB chondrites are typically much smaller. Therefore, employing the IMS-1290 was necessary to measure such samples with smaller mineral grain sizes. Also, over the course of this study, we optimized the analytical configuration for our IMS-1290 measurements to obtain better precision. In the particular case of the FUN CAI *CMS-1*, we performed the ¹⁰Be–¹⁰B analyses with the IMS-6f as well as two different analytical configurations (involving mono- and multicollection) on the IMS-1290. Each of these three analytical methods yielded similar ¹⁰Be–¹⁰B results within the (relatively large) uncertainties, although the multi-collection IMS-1290 configuration resulted in the best precision. Regressing the *CMS-1* data together from the three analytical methods yields an MSWD of ~1 (Fig. 1), indicating that the results from analyses using the two different SIMS instruments and different analytical configurations (mono- versus multi-collection) are consistent with each other.

2.3. SIMS ²⁶Al-²⁶Mg Analyses

The ²⁶Al-²⁶Mg isotope systematics in six CAIs were determined using the Cameca IMS-1280 at UW-Madison using methods similar to those described previously (Ushikubo et al., 2017; Kita et al., 2012). We conducted two sessions, one of which was for two CV CAIs (*Agave* and *Cholla*) and the other was for four CR CAIs (*Dalea*, *Dalea2*, *Creosote*, and *Yucca*). Analytical conditions for each session are described below.

For the first session analyzing CV CAIs, we used the duoplasmatron ion source and prepared four $^{16}O^-$ primary ion beam settings for analyses of melilite (~15 µm, 4 nA and ~7 µm, 50–100 pA), spinel and pyroxene (~10 µm, 1.8 nA), and anorthite (~8 µm, 0.5 nA). The secondary ions $^{24}Mg^+$, $^{25}Mg^+$, $^{26}Mg^+$ and $^{27}Al^+$ were collected under two conditions, depending on the measured phase and necessary spot size: (1) multi-collection of $^{24}Mg^+$, $^{25}Mg^+$, $^{26}Mg^+$ and $^{27}Al^+$ using four Faraday cup (FC) detectors (used to measure the low Al/Mg phases including åkermanite-rich melilite, pyroxene, and spinel with spot sizes > 10 µm) and (2) mono-collection using the axial EM detector for $^{24,25,26}Mg^+$ and one FC for $^{27}Al^+$ that operated by magnetic peak switching (used to measure the high Al/Mg phases including åkermanite-poor melilite and anorthite with spot sizes < 8 µm). For the multi-collection mode, the MRP was set to ~2000 on all four FC detectors by using exit slit widths of ~500 µm. For the mono-collection mode, the MRP was set to ~4000 by using an exit slit width of ~300 µm. These conditions were sufficient to eliminate interferences from molecular and doubly charged ions (e.g., $^{24}MgH^+$, $^{25}MgH^+$, $^{48}Ca^{++}$, $^{52}Cr^{++}$). $^{27}Al^+$ ions were collected by the FC (H'2) with a 10^{10} Ω resistor for both conditions. For the multi-collection mode, three $10^{11}\,\Omega$ resistors were used

for collecting ^{24,25,26}Mg⁺ ions. For the mono-collection mode, ²⁷Al⁺ ions were detected during the measurement of ²⁵Mg⁺. Per cycle, the counting durations for individual ions were 3s for ²⁴Mg⁺ and 10s for ²⁵Mg⁺, ²⁶Mg⁺, and ²⁷Al⁺ ions. The waiting durations were 2s for ²⁴Mg⁺ and 2s for ²⁵Mg⁺, ²⁶Mg⁺, and ²⁷Al⁺ ions. The mass 23.9 was also measured for stabilizing magnetic field for ²⁴Mg⁺ (counting duration = 2s, waiting duration = 1s). For high-precision results, we measured multiple matrix-matched standards with known Mg isotope and Al/Mg ratios to characterize IMF and RSF. The standards include melilite-composition glass standards (Åk₁₅, Åk₂₅, Åk₃₅, Åk₆₅, Åk₇₅, Åk₈₅), natural pure spinel (MgAl₂O₄), pyroxene-composition glass standards with differing Ti content (5–10 wt.% TiO₂), natural plagioclase (Lab1; An₅₉ with 0.1% MgO), and anorthite-composition glass standards (An₁₀₀ with 0.1 wt.% MgO, An₁₀₀ with 1 wt.% MgO).

358359

360361

362363

364

365

366

367

368

369

370

371

372

373374

375

376

377378

379

380

381

382

383

384

385 386

387

388

389

390

391

392

393

394

395

396

397

398

399

400

401 402

403

404 405

406

407

For the second session for CR CAIs, we used the radio-frequency (RF) plasma ion source and prepared five ¹⁶O₂ primary ion beam settings for analyses of melilite (~10 μm, 2 nA), larger pyroxene (~6 μm, 750 pA), spinel and smaller pyroxene (~5 μm, 320 pA), and anorthite (~5 µm, 220 pA and ~3 µm, 23 pA). As for the first session, the secondary ions ²⁴Mg⁺, ²⁵Mg⁺, ²⁶Mg⁺ and ²⁷Al⁺ were collected under two conditions (i.e., multi-collection and monocollection). Analyses of melilite, spinel and pyroxene were performed with the multi-collection mode so that all secondary ions were detected simultaneously on the four FCs with the MRP of ~2000. In this session, we used three lower-noise feedback resistors ($10^{12} \Omega$) for the measurements of ²⁴Mg⁺, ²⁵Mg⁺, and ²⁶Mg⁺ ions to improve the precision of Mg isotope analyses (Fukuda et al., 2021b). For both multi- and mono-collection modes, ²⁷Al⁺ ions were collected by the FC (H'2) with a $10^{11} \Omega$ resistor. For mono-collection mode, the counting and waiting duration for individual ions were the same as those for the first session, except for the counting duration for ²⁴Mg⁺ ions (4s instead of 3s). The MRP was set to ~3000. Similar sets of standards used for the first session were analyzed to characterize IMF and RSF. Additionally, one diopside standard (95AK-6 Di) was used as a bracket standard for analyzing Ti-poor pyroxene. In order to aim the primary ion beam onto small anorthite grains precisely, we employed focused ion beam (FIB) marking to target areas prior to SIMS analyses. FIB marking was performed with the Nova 200 Nanolab FEI at ASU, following procedures described in Hertwig et al. (2019).

For both sessions, a single analysis took ~9–13 min for the multi-collection mode, while those for mono-collection analysis took ~20-30 min for anorthite and ~2 hours for melilite. The typical secondary ion intensity as well as external reproducibility of each running standard are summarized in the Supplementary Materials. Data reduction and error estimation procedures follow those described in Ushikubo et al. (2017). The IMF-corrected Mg isotope ratios (δ^{25} Mg_{DSM3}) of CAI minerals are reported as relative deviations from the Mg reference material DSM3 (Galy et al., 2003). Multiple matrix-matched standards were measured during both sessions to correct for IMF in Mg isotopes, the δ^{25} Mg_{DSM3} values of which, except for the spinel standard, were reported in Kita et al. (2012) and Fukuda et al. (2020). This value for the spinel standard is not available at present so that it is assumed to be 0 to calculate the δ^{25} Mg_{DSM3} values of the unknown spinels. Some anorthite analyses show variation in ²⁷Al/²⁴Mg ratios within a single analysis, which correlate with the excess radiogenic ²⁶Mg (²⁶Mg*). Therefore, we estimated the error correlation coefficient between ²⁷Al/²⁴Mg ratios and the ²⁶Mg* values of individual cycles for these analyses (Supplementary Materials). In order to do that, we characterized the ²⁷Al/²⁴Mg RSF for individual cycles based on the cycle-by-cycle change of ²⁷Al⁺/²⁴Mg⁺ ratios observed for bracket standard analyses. Excess radiogenic ²⁶Mg was calculated using the equation $\delta^{26} \text{Mg*} = [(1 + \delta^{26} \text{Mg}/1000) - (1 + \delta^{25} \text{Mg}/1000)^{1/\beta}] \times 1000$, and the β value of 0.5128 (Davis et al., 2015) was utilized. Uncertainties in δ^{25} Mg_{DSM3} and δ^{26} Mg* values were estimated based on the internal error of individual analyses (2SE) and external reproducibility of the bracket standard analyses (2SD) (see EA1 in Ushikubo et al., 2017 for more details). In addition to these errors, uncertainty in the ²⁷Al/²⁴Mg ratios of the bracket standards determined by EPMA analyses (1%) was also propagated for the error estimation on the ²⁷Al/²⁴Mg ratios. Resulting data are shown in Supplementary Materials.

410 411 412

408 409

2.4. SIMS Oxygen Isotope Analyses

413 414

415

416

417

418

419

420

421

422 423

424

425

426

427

428 429

430

431

432

433

434 435

436 437

We used the CAMECA IMS-1280 for *in-situ* oxygen isotope analyses at the WiscSIMS laboratory at UW-Madison. In situ oxygen isotope analyses of spinel, melilite, pyroxene, and anorthite in CAIs Saguaro, Agave, B4, and TS23 were performed with a Cs⁺ beam during one session, while *Cholla* analyses were completed during a separate session using a different configuration. For the first session, analytical conditions were similar to those reported using three FC configuration (Kita et al., 2010). The primary beam was focused to ~8 µm diameter spot at 0.6 nA. The secondary $^{16}O^{-}$ beam intensity was $\sim 8 \times 10^{8}$ cps. We used a $10^{12} \Omega$ resistor for the FC amplifier board for ¹⁷O. The MRP was set to ~2200 for ¹⁶O and ¹⁸O using 2 detectors on the multi-collection array, and 5000 for ¹⁷O using an axial FC (FC2). The correction for OH- interference on ¹⁷O was checked for each analysis and found to be negligibly small (<0.04‰) except for a few cases. For the second session, analytical conditions were similar to those reported using FC-EM-EM (Ushikubo et al., 2017). The focused primary beam was set to ~3 µm diameter and intensity of ~20 pA. The secondary ions ¹⁶O⁻, ¹⁷O⁻, and ¹⁸O⁻ were detected simultaneously by a FC (¹⁶O⁻), and EMs (¹⁷O⁻ and ¹⁸O⁻) on the multi-collection system. Intensities of ${}^{16}\text{O}^-$ were $\sim 2 \times 10^7$ cps. The contribution of the tailing ${}^{16}\text{OH}^-$ interference to ¹⁷O⁻ signal was corrected by the method of Heck et al. (2009), though the contribution was negligibly small (<0.04‰). For both sessions, San Carlos olivine was used as a standard and bracketed the unknown CAI analyses. Instrumental mass biases were corrected from the analyses of pyroxene (TiO₂: 2%, 10%), melilite (åkermanitic and gehlenitic), anorthite, and spinel standards at the beginning of the session. The 2SD errors for $\Delta^{17}O$ (= $\delta^{17}O - 0.52 \times \delta^{18}O$) were typically ± 0.5 –1.0%. After the SIMS session, SEM images were taken of the analysis spots; only a few visibly overlapped cracks, small inclusions, or were too close to previous oxygen primary analysis spots (expected to result in more ¹⁶O-rich measured compositions due to contamination by this primary beam composition); data from such spots were excluded from further consideration.

438 439

2.5. Isotope Ratio Determination and Isochron Regression

440 441 442

443

444

445

446

447 448

449 450

451

452

453

454 455

456

457

Due to the low concentration of boron in CAIs, detecting boron isotopes with SIMS is challenging. Secondary ¹¹B ions can be as low as a few counts per second in some cases (with ¹⁰B lower than one count per second). As introduced by Telus et al. (2013) for the ¹⁰Be-¹⁰B and ⁶⁰Fe-⁶⁰Ni isotope systems, isotope ratios calculated with low counts must be treated mathematically with care to avoid introducing ratio bias. We tested multiple ratio calculations to determine which generates the true ratio. It has been established that cycle-by-cycle ratio averaging (the 'mean of the ratios') results in a ¹⁰B/¹¹B ratio that is higher than the true value (Telus et al., 2013). Summing the counts of all cycles before taking a ratio, or integrated counts (the 'ratio of the means'), yields a less biased ratio (Ogliore et al., 2011). Integrated counts may still yet be biased if there are cycles in which the counts are 0. The integrated quasi-unbiased approach (Coath et al., 2013) accounts for this by treating each cycle of measurement with the equation: [(10B total counts)/(11B total counts +1)] where the total counts are corrected for the background level of the detector. We used integrated counts to determine all ⁹Be/¹¹B and ¹⁰B/¹¹B isotope ratios and tested the analyses from a few CAIs with the integrated quasiunbiased approach. The two techniques yield isotope ratios that are at most 2% different, which is well within our analytical errors. We encourage others, if dealing with low counting statistics,

to calculate isotope ratios using the techniques of Ogliore et al. (2011) and Coath et al. (2013) to make certain they are not unintentionally introducing bias.

The ¹⁰Be-¹⁰B and ²⁶Al-²⁶Mg isotope York regressions were determined with *IsoplotR* (Vermeesch, 2018; York et al., 2004) and a model 1 fit (which takes into account the analysis uncertainties). The correlated errors shown in Supplementary Materials were *IsoplotR* inputs; however, the error envelope correlations are not plotted in Fig. 1. The mean squared weighted deviation (MSWD) value output by *IsoplotR* is used to assess the degree of over- or underdispersion of the data fit to a linear regression. This value is calculated using the equation:

466
$$MSWD = \frac{1}{N-2} \sum_{i=1}^{N} \frac{(y_i - a - bx_i)^2}{\sigma_{y_i}^2 + b^2 \sigma_{x_i}^2}$$

where a is the inferred intercept of the fit and b is the inferred slope, N is the number of data points in the fit and x_i and y_i are ${}^9\mathrm{Be}/{}^{11}\mathrm{B}$ and ${}^{10}\mathrm{B}/{}^{11}\mathrm{B}$ ratios in our case. To determine the significance of the linear fit, we also calculate the uncertainty of the MSWD. For a linear regression with two free parameters (slope and intercept), the value of the MSWD, if the scatter of points is due to measurement errors with the reported uncertainties, is expected to lie within the range $1\pm2\sigma_{\mathrm{MSWD}}$, where:

$$\sigma_{\text{MSWD}} = \sqrt{\frac{2}{(N-2)}}$$

If the fit yields an MSWD outside this 2-sigma limit (either too high or too low), there is a less than ~5% probability that the data conform to a simple linear model and yet exhibit an MSWD so far from 1; scientific inferences based on that model are statistically inappropriate (Wendt and Carl, 1991).

Table 3
The results of ¹⁰Be-¹⁰B isochron regressions for the CAIs studied here.

Meteorite	type	CAI sample	CAI-type	[Be] range (ng/g)	[B] range (ng/g)	¹⁰ Be/ ⁹ Be (×10 ⁻⁴)	2SE (×10 ⁻⁴)	¹⁰ B/ ¹¹ B	2SE	n	MSWD	1+2σ _{MSWE}
NWA 6991	CV3 _{ox}	B4	CTA	494–915	24-1958	6.7	2.2	0.2435	0.0022	8	0.6	2.2
Allende	CV3.6 _{ox}	CMS-1	FUN B	31-1048	14-903	1.8	3.2	0.251	0.002	18	0.7	1.7
Allende	$CV3.6_{ox}$	TS68	CTA	348-497	6-215	5.7	2.2	0.2569	0.0066	7	1	2.3
Allende	$CV3.6_{ox}$	TS23A	B1	220-451	2-162	6.1	2.2	0.2488	0.0064	9	0.9	2.1
NWA 7891	CV3 _{ox} *	ZT4	CTA	650-2954	6-600	7.3	1.0	0.2391	0.0054	9	0.9	2.1
NWA 3881	$CV3_{ox}$	ZT7	CTA	230-965	6-802	5.3	2.6	0.2499	0.0058	6	1.3	2.3
NWA 5028	CV3 _{red} *	Agave	B2	108-2377	21-1766	11.6	4.6	0.2463	0.004	6	1.0	2.4
NWA 5028	CV3 _{red} *	Cholla	FTA	118-722	21-698	7.8	6.6	0.2504	0.0044	4	0.2	3
NWA 5508	CV3 _{red} *	Saguaro	CTA	465-827	11-234	8.1	1.5	0.2387	0.0014	9	0.8	2.1
Leoville	$CV3_{red}$	ZT1	B1	340-1339	11-111	9	4.3	0.2504	0.0091	9	0.6	2.1
Vigarano	$CV3_{red}$	3137	FoB	170-815	51-917	7.2	3.0	0.2498	0.0019	10	0.8	2
DaG 027	CO3	Anning	CTA-like	91-297	4-448	8.5	3.0	0.2493	0.0079	6	1.1	2.4
DaG 005	CO3	Bascom	CTA-like	112-727	4-110	8.8	3.4	0.2489	0.0088	4	0.3	3
DaG 027	CO3	Goeppert	CTA-like	113-222	6-32	6.9	5.2	0.2539	0.0142	3	0.1	3.8
DaG 027	CO3	Jemison	CTA-like	20-433	4-17	7.9	3.0	0.2554	0.0156	5	1.3	2.6
DaG 027	CO3	Krafft	CTA-like	125-430	9–14	10.9	5.6	0.256	0.022	6	2.0	2.4
NWA 7892	CO3.05	Mesquite	CTA-like	7-547	8-62	9.8	6.6	0.2481	0.009	6	0.8	2.4
DaG 005	CO3	Mitchell	CTA-like	36-202	5-10	8.7	7.6	0.2544	0.0246	3	0.01	3.8
DOM 08006	CO3.00	31-2	grossite-rich	156-555	24-336	14.6	6.6	0.2451	0.0038	9	0.9	2.1
NWA 801	CR2	Cereus	CTA-like	865-1216	356-2408	9.5	7.6	0.2504	0.0013	5	0.9	2.6
MIL 090657	CR2.7	Creosote	CTA-like	518-977	28-84	2.1	6.4	0.2562	0.0124	8	0.4	2.2
Shişr 033	CR2	Dalea	CTA-like	1000– 2350	17-8714	7.3	1.4	0.245	0.0012	5	0.2	2.6
NWA 801	CR2	Palo Verde	melilite grain	382-633	83–151	10.7	6.6	0.2457	0.0014	5	0.9	2.6
MIL 090657	CR2.7	Yucca 5	CTA-like	365–527	16–54	8.7	3.4	0.2438	0.0082	5	0.4	2.6
Isheyevo	CH/CB	Isheyevo CAIs	mel-rich	82–746	6–195	8.6	2.8	0.2427	0.0062	16	1.4	1.8

^{*}We re-classified or sub-classified these chondrites, see Supplementary Materials.

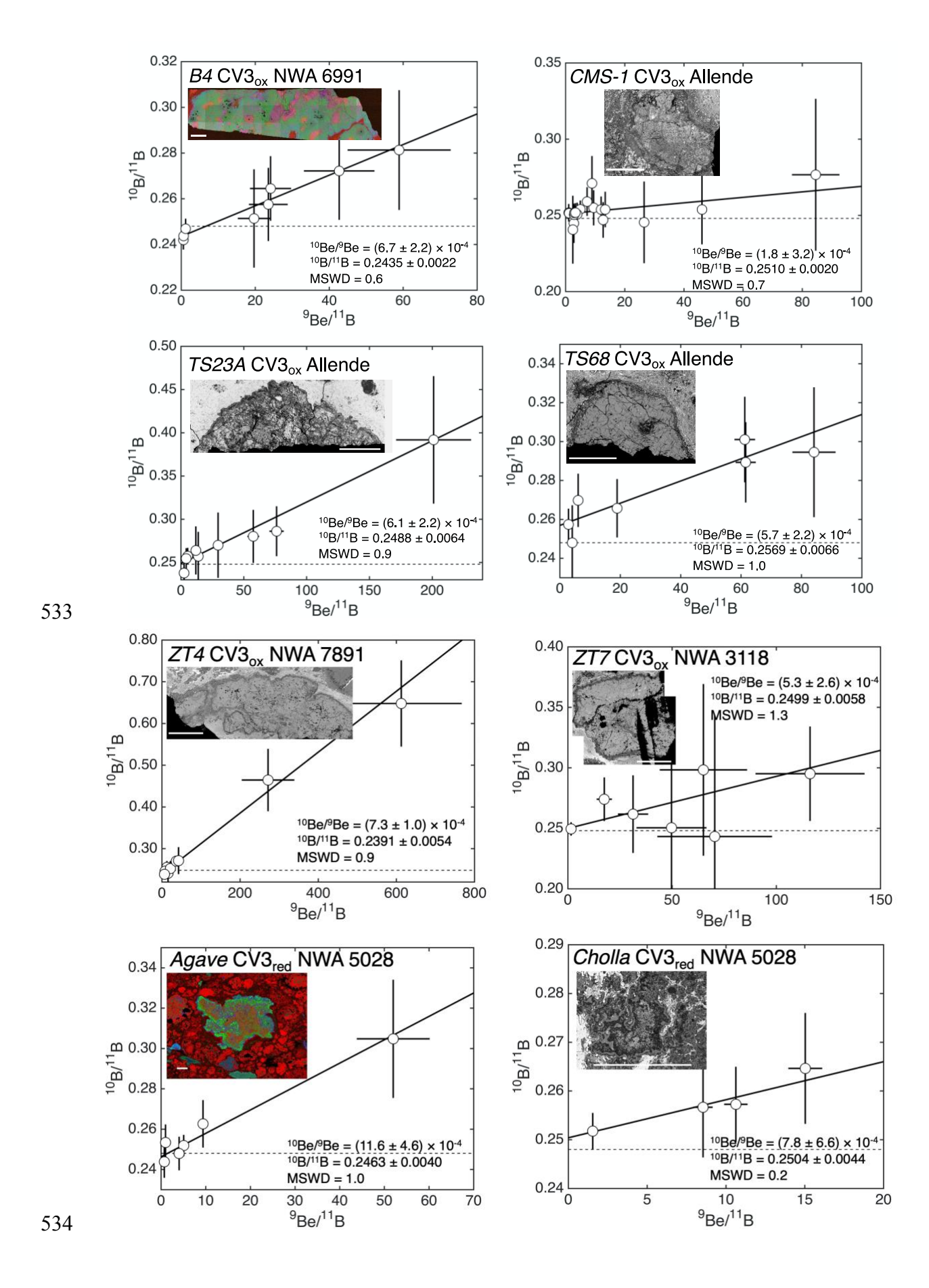
3.1. Twenty-five ¹⁰Be-¹⁰B CAI isochron regressions

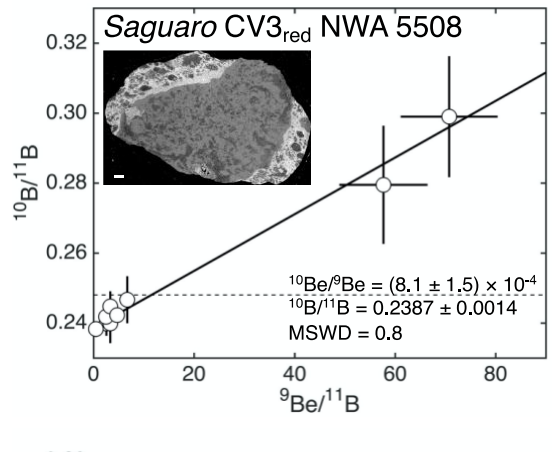
The 10 Be $^{-10}$ B isochron regressions and data for each of the CAIs studied here are shown in Table 3. Figure 1 shows the 10 Be $^{-10}$ B isochron plots along with BSE images of the CAIs. The CAIs from CV3_{ox} (n=6) and CV3_{red} (n=5) chondrites record best-fit initial 10 Be/ 9 Be in the range $(1.8-7.3) \times 10^{-4}$ and $(7.1-11.6) \times 10^{-4}$, respectively. The CO3 CAIs (n=8) record best-fit initial 10 Be/ 9 Be in the range $(6.9-14.6) \times 10^{-4}$. This is the first study in the refereed literature to report 10 Be $^{-10}$ B systematics of CR2 CAIs. CR2 CAIs (n=5) record best-fit initial 10 Be/ 9 Be in the range $(2.1-10.7) \times 10^{-4}$. Combining the CH/CB CAI (n=5) 10 Be $^{-10}$ B analyses into a single isochron regression yields an initial 10 Be/ 9 Be = $(8.6 \pm 2.8) \times 10^{-4}$ (MSWD = 1.4). We measured 10 Be $^{-10}$ B isotope systematics in 29 CAIs but calculated 25 isochron regressions because we combined the 5 CH/CB CAIs into a single multi-CAI regression; the small size of the CH/CB CAIs and their low Be/B ratios result in poor single CAI regressions.

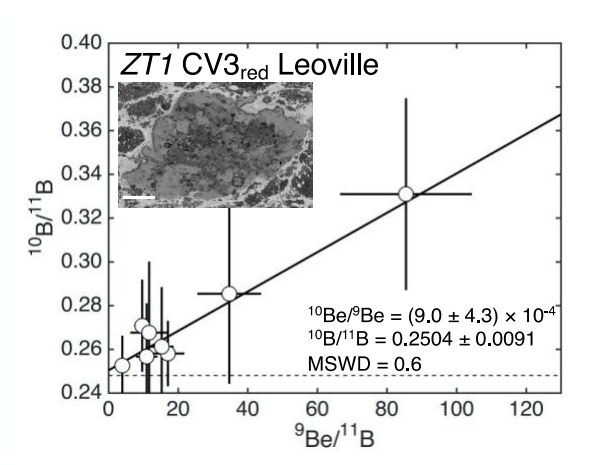
We separately describe the results of three especially interesting CAIs: FoB CAI 3137 from CV3_{red} Vigarano (MacPherson et al., 2017), FUN CAI CMS-1 from CV3.6_{ox} Allende (Williams et al., 2017), and UN CAI 31-2 from CO3.00 Dominion Range (DOM) 08006 (Simon et al., 2019b). The FoB CAI 3137 has an initial ${}^{10}\text{Be}/{}^{9}\text{Be} = (7.2 \pm 3.0) \times 10^{-4}$ and an initial $^{10}B/^{11}B$ ratio of 0.250 ± 0.002 (MSWD = 0.8). The FUN CAI *CMS-1* is inferred to have been a forsterite-bearing inclusion before thermal processing (Mendybaev et al., 2017) and records ${}^{10}\text{Be}/{}^{9}\text{Be} = (1.8 \pm 3.2) \times 10^{-4} \text{ with an initial } {}^{10}\text{B}/{}^{11}\text{B} = 0.251 \pm 0.002 \text{ (MSWD} = 0.7).}$ The large uncertainty on the isochron slope leads us to report an upper limit (2SE) on the inferred initial 10 Be/ 9 Be ratio for CMS-1 of $< 5.0 \times 10^{-4}$. The UN CAI 31-2 (Simon et al., 2019a; Simon et al., 2019b) yields an initial ${}^{10}\text{Be}/{}^{9}\text{Be} = (14.6 \pm 6.6) \times 10^{-4}$ and an initial ${}^{10}\text{B}/{}^{11}\text{B}$ ratio of 0.245 ± 0.004 (MSWD = 0.9). It is noted that in this CAI, the phase that was analyzed was grossite (CaAl₄O₇) rather than melilite. Because standards for grossite are not available, we used NIST standards in this case. We know that matrix-matched melilite-composition glass standards yield calibrations similar to those from NIST 610, 612, and 614 standards (Dunham et al., 2020; Fukuda et al., 2018) and so consider it reasonable that grossite composition would behave similarly to melilite-composition and NIST standards when determining Be/B abundances. Even if this is not the case, the analytical uncertainties from counting statistics are likely larger than any matrix-induced calibration effects.

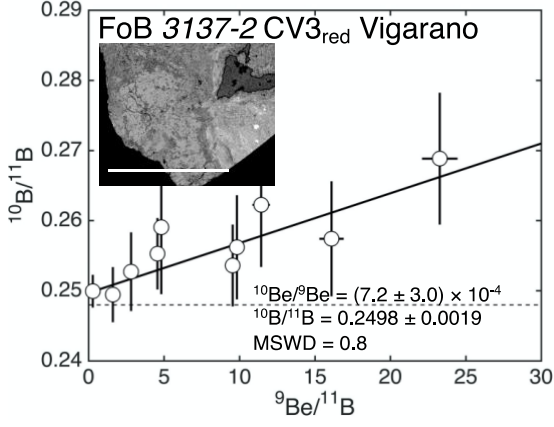
3.2. Five ²⁶Al-²⁶Mg CAI isochron regressions

In addition to 10 Be $^{-10}$ B systematics, we measured the 26 Al $^{-26}$ Mg isotope systematics in five selected CAIs that were chosen because they display a range of textural and mineralogical characteristics. The 26 Al $^{-26}$ Mg systematics in these CAIs are consistent with a canonical initial 26 Al $^{/27}$ Al ratio $\sim 5 \times 10^{-5}$ (Jacobsen et al., 2008): CV3red CAIs *Agave* and *Cholla* recorded initial 26 Al $^{/27}$ Al = $(4.98 \pm 0.05) \times 10^{-5}$ with $(\delta^{26}$ Mg* = -0.14 ± 0.05 , 2SE; MSWD = 3.3) and $(5.22 \pm 0.28) \times 10^{-5}$ with $(\delta^{26}$ Mg* = -0.071 ± 0.100 , 2SE; MSWD = 0.8), respectively. The CR2 CAIs *Dalea*, *Creosote*, and *Yucca* recorded 26 Al $^{/27}$ Al = $(4.54 \pm 0.45) \times 10^{-5}$ with $(^{26}$ Mg* = -0.008 ± 0.128 , 2SE; MSWD = 1.7), $(4.68 \pm 0.15) \times 10^{-5}$ with $(\delta^{26}$ Mg* = -0.076 ± 0.062 , 2SE; MSWD = 1.0), and $(4.37 \pm 0.35) \times 10^{-5}$ with $(\delta^{26}$ Mg* = 0.101 ± 0.110 , 2SE; MSWD = 1.6), respectively. We measured the rim anorthite in CAI *Creosote*, which was canonical and was included as part of the well-behaved isochron regression for this CAI (Fig. 2). However, we also measured the rim anorthite in CAI *Yucca* (Supplementary Materials), which shows no resolvable 26 Mg excess and is not included as part of the isochron regression for other phases from the interior of this CAI.

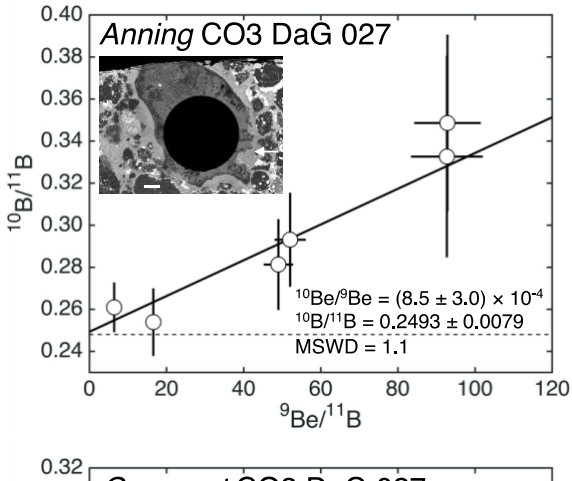


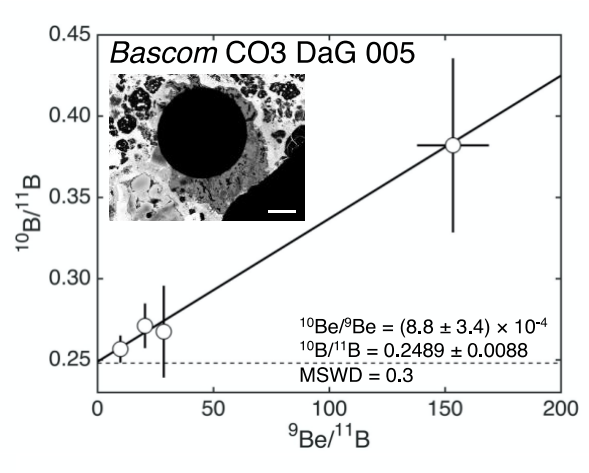


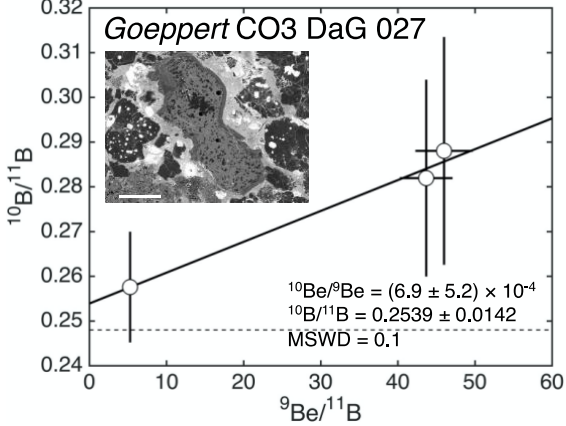


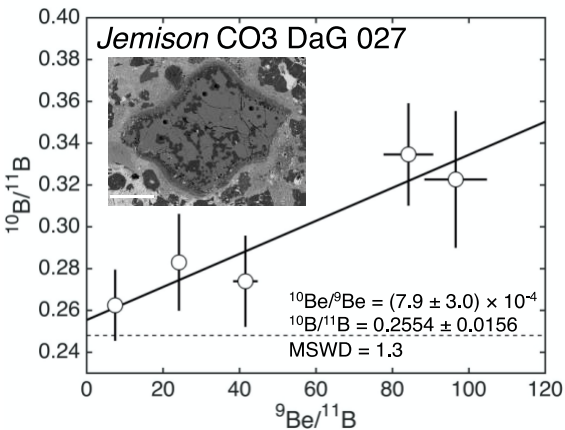


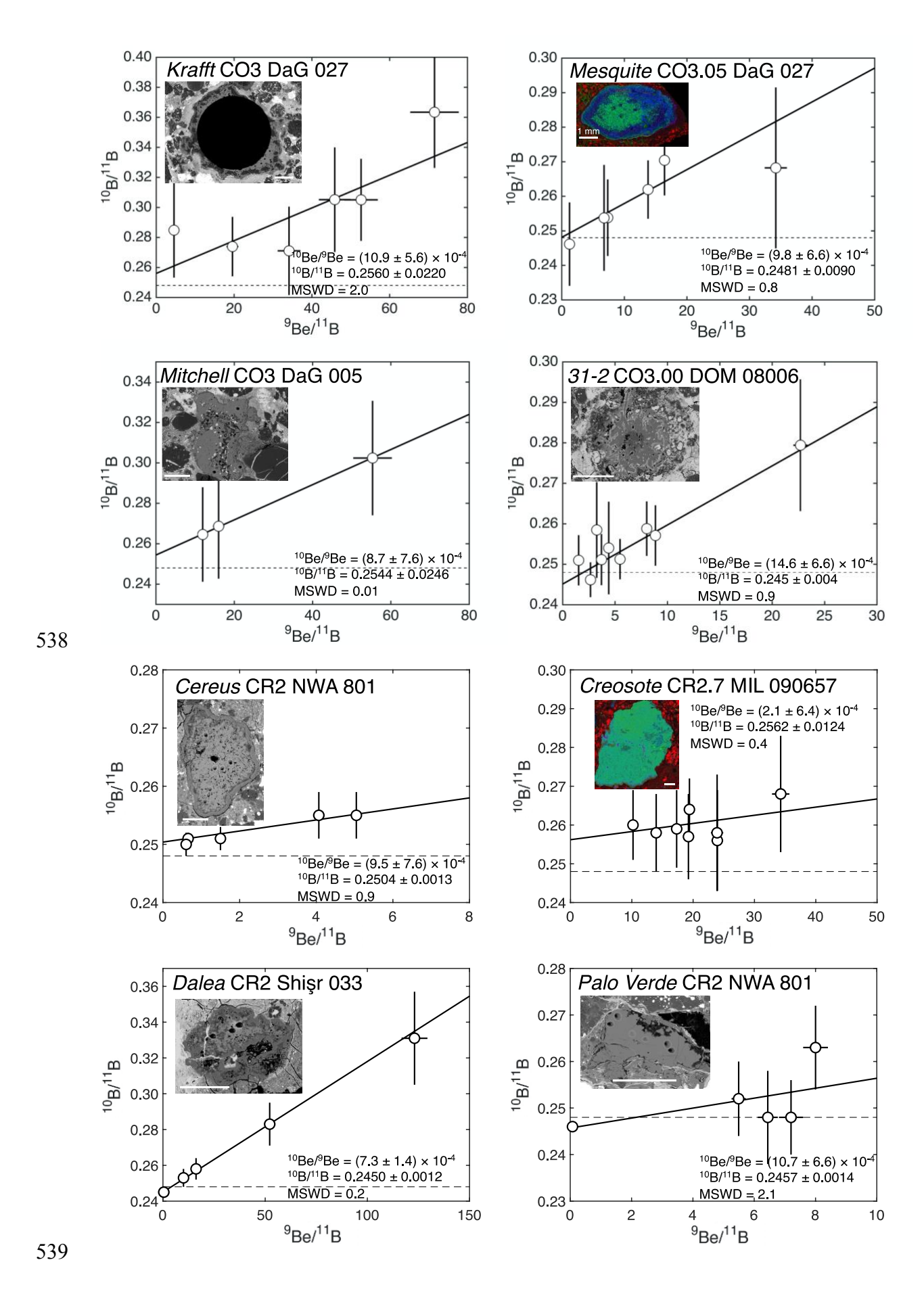












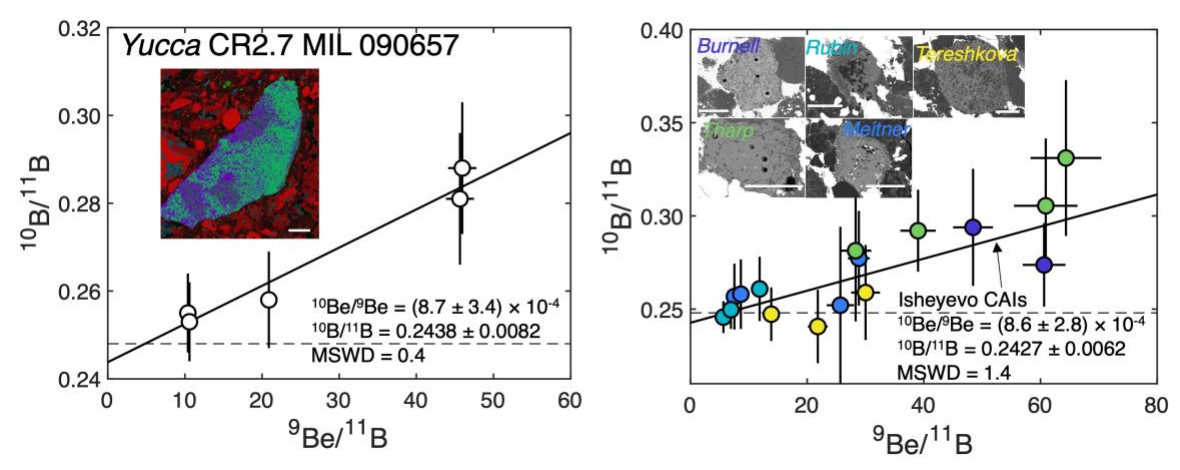


Fig. 1. Twenty-five ¹⁰Be–¹⁰B isochron regressions. The labels in the upper left indicate the CAI name and chondrite name, while the initial ¹⁰Be/⁹Be and ¹⁰B/¹¹B ratios and MSWD are shown in the lower right. Each plot includes an image of the CAI; some are BSE images with visible SIMS pits and others are element maps (where: Red=Mg, Green=Ca, Blue=Al); the white bars indicate the scale of the image; CV3 scale bars are 1 mm while non-CV3 scale bars are 100 μm, unless otherwise indicated. CAIs *Anning*, *Bascom*, and *Krafft* have large microdrill holes because they were measured previously for Ti isotopes (Render et al., 2019). The horizontal dashed line in each plot is the chondritic value for the ¹⁰B/¹¹B ratio (Zhai et al., 1996). Uncertainties are 2σ. See Supplementary Materials for more detailed images and SIMS pit locations.

Additionally, we measured an inclusion ~50 μ m away from CAI *Dalea*, called *Dalea2*, which together were originally thought to be a single inclusion. Inclusion *Dalea2* is composed of spinel nodules surrounded by anorthite and Ca-rich pyroxene. *Dalea2* recorded 26 Al/ 27 Al = $(0.43 \pm 0.26) \times 10^{-5}$ and $(\delta^{26}\text{Mg*} = 0.22 \pm 0.07, 2\text{SE}; \text{MSWD} = 1.6)$ (see Supplemental Materials). It is beyond the scope of this paper to discuss CAI rim Al-Mg chronology and CAI *Dalea2* results in detail, due to our focus on ^{10}Be .

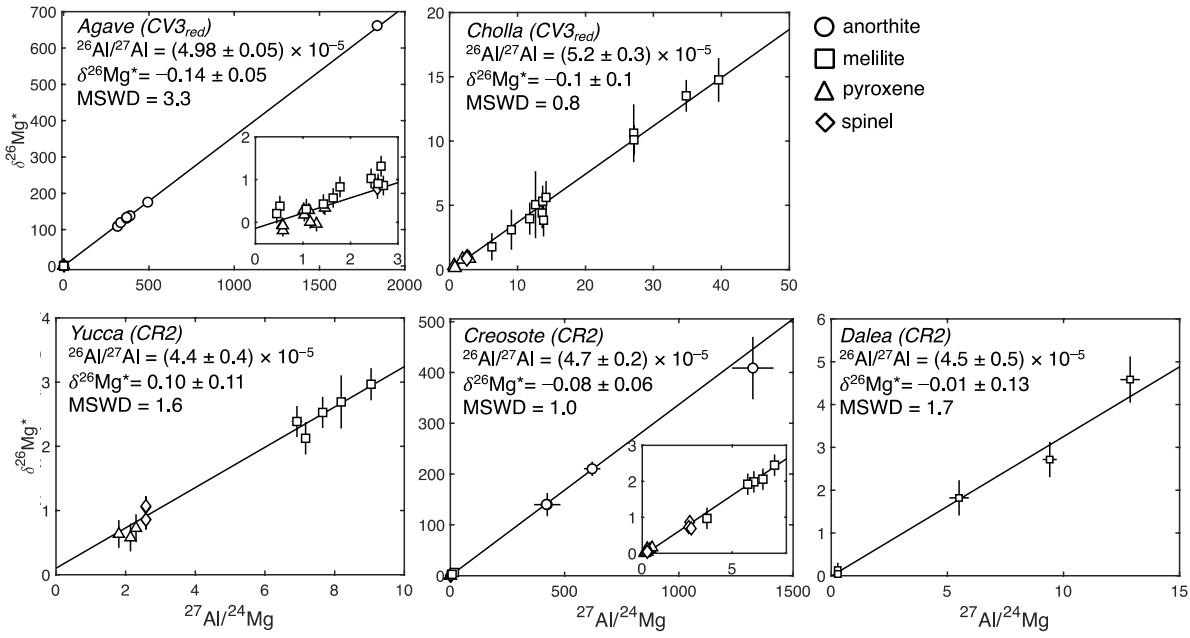


Fig. 2. 26 Al $^{-26}$ Mg isochrons for 5 CAIs, with insets in two cases to show the data more clearly for phases with low Al/Mg ratios. All uncertainties are 2σ .

3.3. Oxygen Isotope Compositions in Five CAIs

We measured the oxygen isotope compositions of spinel, melilite, pyroxene, and anorthite in five CAIs (*B4*, *Cholla*, *TS23*, *Agave*, and *Saguaro*) (Fig. 3). Most of the data in these CAIs have oxygen isotope compositions that lie along the Carbonaceous Chondrite Anhydrous Mineral (CCAM) line; the few exceptions are *B4* anorthite and melilite and *Cholla* melilite. All CAIs have ^{16}O -rich spinel and pyroxene, ranging from $\Delta^{17}\text{O} = -24\%$ to -20%. The CAIs have distinct oxygen isotope distributions among the minerals melilite and anorthite. CAIs, except for *Cholla*, have ^{16}O -poor melilite with $\Delta^{17}\text{O}$ ranging from -1% to -3%. Fluffy type A (FTA) CAI *Cholla* shows melilite ranging in $\Delta^{17}\text{O}$ from -24% to -7%; this variation correlates with Åk content which ranges from 10 to 20 mol%. With respect to anorthite, B1 CAI *TS23* and compact type A (CTA) CAI *B4* are ^{16}O -poor while the B2 CAIs, *Agave* and *Saguaro*, have anorthite ranging in $\Delta^{17}\text{O}$ from -4% to -20%.

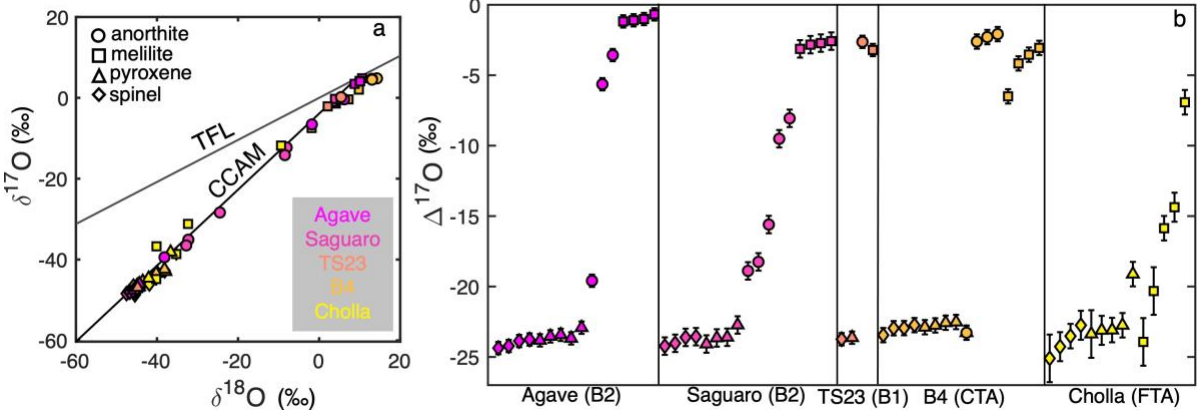


Fig. 3. Oxygen isotope compositions of 5 CAIs. CAIs Agave and Cholla are from NWA 5028 (CV3_{red}), CAI Saguaro is from NWA 5508 (CV3_{red}), CAI B4 is from NWA 6991 (CV3_{ox}), and CAI TS23 is from Allende (CV3_{ox}). Different symbols indicate the different mineral phases analyzed (spinel = diamond; melilite = square; pyroxene = triangle; anorthite = circle) and the colors represent the CAI as indicated in panel (b) (pink = Agave; red = Saguaro; orange = B4; yellow = Cholla). Uncertainties are 2σ .

4. DISCUSSION

4.1. Uniform ¹⁰Be distribution recorded in CAIs?

We measured ¹⁰Be–¹⁰B isotopic systematics in 29 CV3, CO3, CR2, and CH/CB CAIs, from which we determined 25 isochron regressions (the data for the 5 CH/CB CAIs were regressed together as only a few analyses on phases with low Be/B ratios were possible on each CAI). They record initial ¹⁰Be/⁹Be ratios in the range (1.8–14.6) × 10⁻⁴, but 96% (24 of the 25 CAI isochrons) recorded initial ¹⁰Be/⁹Be of ~ (7–8) × 10⁻⁴, within the uncertainties (Figs. 1, 4, and 5). The isochron regressed from the FUN CAI CMS-1 data is the only one that yields an initial ¹⁰Be/⁹Be that does not agree with this mean value; we consider it separately below and focus here on the other 24 CAI isochrons. As can be seen in Fig. 4, there is not a significant or systematic difference between the ¹⁰Be/⁹Be ratios inferred for CV3_{ox}, CV3_{red}, CR2, CO3 or CH/CB CAIs, or between different petrologic types of CAIs (i.e., condensates versus igneous, or Type A versus Type B). Because we are testing whether ¹⁰Be was distributed homogeneously or heterogeneously among CAIs, with the goal of determining the origin of ¹⁰Be, we assess whether our CAI data are primarily consistent with a single initial ¹⁰Be/⁹Be ratio. One approach is to evaluate statistically if the data are part of a single population. We find that the weighted average ¹⁰Be/⁹Be value from our 24 CAI isochron regressions is (7.5)

 $\pm\,0.3) \times 10^{-4}$ with an MSWD = 0.8. Considering that N = 24, the maximum MSWD for these data to define a single population is 1.5, which is higher than the MSWD of the data group. This indicates that all CAIs analyzed here to obtain these 24 CAI isochron regressions are indeed part of the same population characterized by a homogeneous initial 10 Be/ 9 Be value.

 Another approach to quantifying the 10 Be/ 9 Be homogeneity, or lack thereof, in the CAI dataset is to determine its probability density distribution. If only one probability density peak is apparent, then the data conform to a single value. If we consider our full dataset of 10 Be/ 9 Be values based on 25 CAI isochron regressions, the probability density distribution, calculated using MATLAB, defines a single peak at 10 Be/ 9 Be = 7.4×10^{-4} (FWHM = 4.1), where the uncertainty is defined by the full width at half maximum (FWHM) of the curve (Fig. 5); including (n = 25) or not including (n = 24) the data for the FUN CAI CMS-1 in the probability density function does not affect the outcome. There are no other significant peaks on this curve. There is a slight deviation around 10 Be/ 9 Be $\sim 10 \times 10^{-4}$, however this does not alter the interpretation that these data are statistically distributed around a single value.

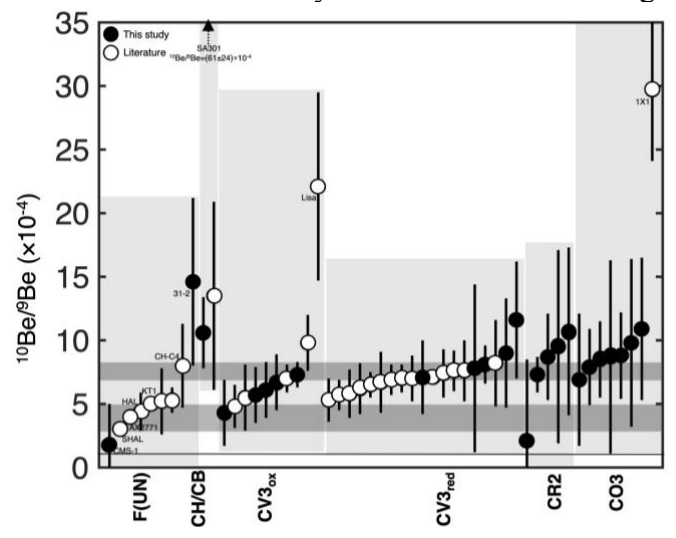


Fig. 4. The 10 Be/ 9 Be ratios inferred from 54 CAI isochron regressions (this study; McKeegan et al., 2000; Sugiura et al., 2001; Marhas et al., 2002; MacPherson et al., 2003; Chaussidon et al., 2006; Liu et al., 2009; Liu et al., 2010; Wielandt et al., 2012; Gounelle et al., 2013; Srinivasan and Chaussidon, 2013; Sossi et al., 2017; Fukuda et al., 2019; Mishra and Marhas, 2019; Fukuda et al., 2021a). Data for FUN and UN CAIs are shown on the left-most side of the plot; other data are grouped according to the different carbonaceous chondrite classes that the CAIs come from. The vertical light gray boxes highlight these different groups of CAIs: F(UN), CH/CB, CV3_{ox}, CV3_{red}, CR2, and CO3. The upward pointing arrow indicates CAI SA301, which has a high 10 Be/ 9 Be of $(6.1 \pm 2.8) \times 10^{-3}$ (Fukuda et al., 2019), well above the maximum value on this plot. The horizontal dark gray bars indicate the 10 Be/ 9 Be values for the normal group (10 Be/ 9 Be $\sim (7-8) \times 10^{-4}$) and the FUN group (10 Be/ 9 Be $\sim (3-5) \times 10^{-4}$) of CAIs. Some CAI data points are labeled. Uncertainties are 2σ .

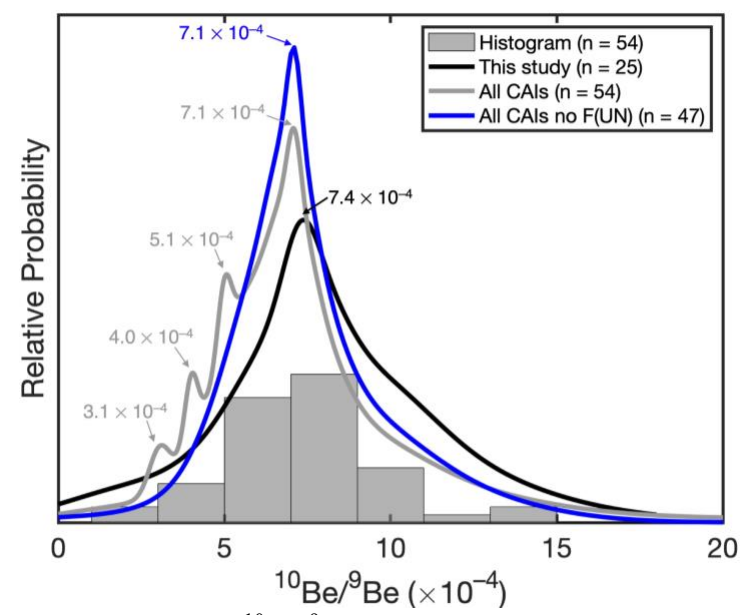


Fig. 5. Probability density plot of initial 10 Be/ 9 Be ratios inferred in CAIs. The probability density distribution of values from this study is shown in black, that of values from this study combined with those from the literature is shown in gray, and that of values from this study combined with literature values but excluding FUN CAIs and PLACs is shown in blue. The histogram with gray bars is another way to present the combined data. We did not consider any isochron regressions from the literature that had high MSWD. The data from our study are distributed about a single peak with 10 Be/ 9 Be = 7.4×10^{-4} (black curve). The combined data from this study and the literature are predominantly distributed about a single peak at 10 Be/ 9 Be = 7.1×10^{-4} , however there are smaller peaks at 3.1, 4.0, and 5.1×10^{-4} (gray curve). The combined data from this study and the literature, but not including FUN CAIs, are also distributed about a single peak at 10 Be/ 9 Be = 7.1×10^{-4} (blue curve). The gray and blue distributions include three CAIs with 10 Be/ 9 Be > 25×10^{-4} ; including them does not alter the probability density distribution so we limit the plot axis to 20×10^{-4} for clarity.

4.1.1. Outlier FUN CAI CMS-1.

 The only CAI from this study that recorded an initial $^{10}\text{Be}/^9\text{Be}$ ratio outside of and lower than $\sim (7-8) \times 10^{-4}$ is FUN CAI *CMS-1*. This is consistent with previous reports of lower $^{10}\text{Be}/^9\text{Be}$ in other FUN CAIs (Liu and Keller, 2017; Wielandt et al., 2012; MacPherson et al., 2003). Here we compare *CMS-1* to UN CAI *31-2* because they are both $^{26}\text{Al-poor}$ CAIs and both have nucleosynthetic isotope anomalies. The difference between them is that *CMS-1* has a low $^{10}\text{Be}/^9\text{Be}$ ratio of $<5 \times 10^{-4}$ and highly mass fractionated isotope signatures while 31-2 has $^{10}\text{Be}/^9\text{Be}$ ratio of $(14.6 \pm 6.6) \times 10^{-4}$ and no mass-dependent fractionations. The isotope compositions in FUN CAI *CMS-1* are indicative of melting and evaporation events as well as the presence of nuclear anomalies (Williams et al., 2017). In contrast, UN CAI 31-2, which has nuclear anomalies but no mass-dependent fractionations, likely did not experience significant thermal processing after condensation (Simon et al., 2019b). Due to these similarities and differences between *CMS-1* and 31-2, we suggest the possibility that $^{26}\text{Al-poor}$ FUN CAI *CMS-1* has a distinct $^{10}\text{Be}-^{10}\text{B}$ signature due to the thermal processing it experienced (that also produced the mass-dependent fractionations), resulting in an apparently lower initial $^{10}\text{Be}/^9\text{Be}$ value.

We can also compare FUN CAI *CMS-1* to FoB CAI *3137-1* because it is proposed that the starting composition of *CMS-1* was an FoB-like composition (Mendybaev et al., 2017). FoB CAI *3137-1* has a 10 Be/ 9 Be ratio of $(7.1 \pm 2.9) \times 10^{-4}$; CAI *CMS-1* could have started out

like CAI 3137-1, but subsequently experienced an evaporation event. A furnace experiment (Mendybaev et al., 2017) was specifically conducted using the proposed FoB starting composition of FUN CAI CMS-1. This study concluded that, after an hour at 1900°C, 80% of SiO₂ and 85% of MgO escaped from the residue by evaporation. It is unknown how exactly B would behave during such an event because evaporation and diffusion coefficients have not been experimentally determined. The loss of some B from the system is possible during heating and evaporation; however, it is noted that while B is relatively volatile (it has a 50% condensation temperature ~635°C, lower than Mg and Si; Lodders, 2003), it is also slow to diffuse (it has been shown to diffuse at about the same rate as Si in granitic compositions; Baker 1992; Chakraborty et al. 1993; Hervig et al. 2002). So, if Si isotopes are disturbed by evaporation, then B isotopes will be too. Beryllium likely would not diffuse from a melt due to its lower vapor pressure, even though it diffuses more quickly than B. Finally, for the ¹⁰Be–¹⁰B systematics in a CAI to be affected by evaporation, the B would need to be lost before ¹⁰Be had fully decayed away. To model this process and assess its plausibility, we assume a hypothetical CAI with 10 Be/ 9 Be $\sim 7 \times 10^{-4}$ and subtract B in an attempt to reproduce a FUN CAI isochron regression with an acceptable MSWD. More specifically, we assume that the hypothetical CAI is similar to CAI *Dalea*, which records ${}^{10}\text{Be}/{}^{9}\text{Be} = (7.3 \pm 1.4) \times 10^{-4} \text{ with } {}^{10}\text{B}/{}^{11}\text{B} = 0.2450 \pm 1.4 \times 10^{-4} \text{ with } {}^{10}\text{B}/{}^{11}\text{B} = 0.2450 \pm 1.4 \times 10^{-4} \text{ with } {}^{10}\text{B}/{}^{11}\text{B} = 0.2450 \pm 1.4 \times 10^{-4} \text{ with } {}^{10}\text{B}/{}^{11}\text{B} = 0.2450 \pm 1.4 \times 10^{-4} \text{ with } {}^{10}\text{B}/{}^{11}\text{B} = 0.2450 \pm 1.4 \times 10^{-4} \text{ with } {}^{10}\text{B}/{}^{11}\text{B} = 0.2450 \pm 1.4 \times 10^{-4} \text{ with } {}^{10}\text{B}/{}^{11}\text{B} = 0.2450 \pm 1.4 \times 10^{-4} \text{ with } {}^{10}\text{B}/{}^{11}\text{B} = 0.2450 \pm 1.4 \times 10^{-4} \text{ with } {}^{10}\text{B}/{}^{11}\text{B} = 0.2450 \pm 1.4 \times 10^{-4} \text{ with } {}^{10}\text{B}/{}^{11}\text{B} = 0.2450 \pm 1.4 \times 10^{-4} \text{ with } {}^{10}\text{B}/{}^{11}\text{B} = 0.2450 \pm 1.4 \times 10^{-4} \text{ with } {}^{10}\text{B}/{}^{11}\text{B} = 0.2450 \pm 1.4 \times 10^{-4} \text{ with } {}^{10}\text{B}/{}^{11}\text{B} = 0.2450 \pm 1.4 \times 10^{-4} \text{ with } {}^{10}\text{B}/{}^{11}\text{B} = 0.2450 \pm 1.4 \times 10^{-4} \text{ with } {}^{10}\text{B}/{}^{11}\text{B} = 0.2450 \pm 1.4 \times 10^{-4} \text{ with } {}^{10}\text{B}/{}^{11}\text{B} = 0.2450 \pm 1.4 \times 10^{-4} \text{ with } {}^{10}\text{B}/{}^{11}\text{B} = 0.2450 \pm 1.4 \times 10^{-4} \text{ with } {}^{10}\text{B}/{}^{11}\text{B} = 0.2450 \pm 1.4 \times 10^{-4} \text{ with } {}^{10}\text{B}/{}^{11}\text{B} = 0.2450 \pm 1.4 \times 10^{-4} \text{ with } {}^{10}\text{B}/{}^{11}\text{B} = 0.2450 \pm 1.4 \times 10^{-4} \text{ with } {}^{10}\text{B}/{}^{11}\text{B} = 0.2450 \pm 1.4 \times 10^{-4} \text{ with } {}^{10}\text{B}/{}^{11}\text{B} = 0.2450 \pm 1.4 \times 10^{-4} \text{ with } {}^{10}\text{B}/{}^{11}\text{B} = 0.2450 \pm 1.4 \times 10^{-4} \text{ with } {}^{10}\text{B}/{}^{11}\text{B} = 0.2450 \pm 1.4 \times 10^{-4} \text{ with } {}^{10}\text{B}/{}^{11}\text{B} = 0.2450 \pm 1.4 \times 10^{-4} \text{ with } {}^{10}\text{B}/{}^{11}\text{B} = 0.2450 \pm 1.4 \times 10^{-4} \text{ with } {}^{10}\text{B}/{}^{11}\text{B} = 0.2450 \pm 1.4 \times 10^{-4} \text{ with } {}^{10}\text{B}/{}^{11}\text{B} = 0.2450 \pm 1.4 \times 10^{-4} \text{ with } {}^{10}\text{B}/{}^{11}\text{B} = 0.2450 \pm 1.4 \times 10^{-4} \text{ with } {}^{10}\text{B}/{}^{11}\text{B} = 0.2450 \pm 1.4 \times 10^{-4} \text{ with } {}^{10}\text{B}/{}^{11}\text{B} = 0.2450 \pm 1.4 \times 10^{-4} \text{ with } {}^{10}\text{B}/{}^{11}\text{B} = 0.2450 \pm 1.4 \times 10^{-4} \text{ with } {}^{10}\text{B}/{}^{11}\text{B} = 0.2450 \pm 1.4 \times 10^{-4} \text{ with$ 0.0012, has B concentrations ranging from 17 to 8,000 ppb (n=5), and defines a ¹⁰Be-¹⁰B isochron with MSWD = 0.2 (Fig. 1; black line in Fig. 6). We consider that initially at t = 0 all five data points for this hypothetical *Dalea*-like CAI in a ¹⁰Be–¹⁰B isochron plot are arrayed along a horizontal line with ${}^{10}B/{}^{11}B = 0.2450$; we then assume that ${}^{10}Be$ decays for 2 Ma, at which point the CAI undergoes partial melting and diffusion of B occurs, such that B is lost when it diffuses to the CAI surface. The amount of B lost from each analysis point likely depends on the proximity to the surface, but just to illustrate the process we make a simplistic assumption that the same amount of B is lost from each point. Finally, the remaining ¹⁰Be decays and the ${}^{10}B/{}^{11}B$ is not homogenized. When we remove ~ 12 ppb of B from each data point, the partially melted *Dalea*-like CAI then records an apparent 10 Be/ 9 Be = $(4.4 \pm 0.6) \times$ 10^{-4} with 10 B/ 11 B = 0.2456 ± 0.0012 and MSWD = 2.6 (upper limit of an acceptable MSWD for a valid isochron given n = 5 is 2.63) (gray line in Fig. 6). Because we can hypothetically produce a FUN CAI-like ¹⁰Be–¹⁰B isochron regression by partially removing B from a normal CAI, we suggest that this mechanism is a possible explanation for the low initial ¹⁰Be/⁹Be ratios found in FUN CAIs, which underwent enough melting and evaporation to produce large isotope fractionations in elements like Mg and Si.

662

663

664665

666

667

668

669

670

671

672673

674

675

676

677

678

679

680

681

682

683 684

685

686 687

688

689 690

691

692

693

694

695 696

697

698

699

700

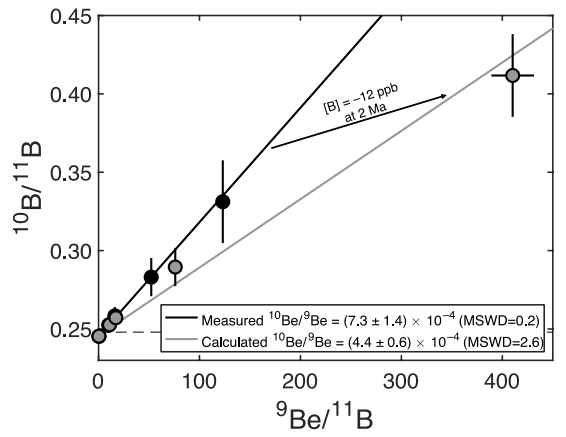


Fig. 6. Plot showing the result of a model calculation illustrating the effect of partial B removal, likely from diffusion upon partial melting, from a hypothetical *Dalea*-like normal CAI. The data for the *Dalea* CAI are shown as the black circles, and the initial ¹⁰Be–¹⁰B isochron for this CAI is shown as the black line. After 2 Ma of ¹⁰Be decay, we subtract 12 ppb of B from each data point. Finally, we allow the complete decay of the remaining ¹⁰Be in this CAI. The result

is an isochron with an apparently lower slope similar to that of some FUN CAIs, i.e., 10 Be/ 9 Be = $(4.4 \pm 0.6) \times 10^{-4}$ (gray line and data points); the original data points move upwards and to the right. The intercept of the original data does not change resolvably after B is removed. The calculated isochron has MSWD = 2.6 (which is still within the range allowed for a valid isochron for n=5 data points). The horizontal dashed line is the chondritic value for the 10 B/ 11 B ratio (Zhai et al., 1996). Plotted uncertainties are 2σ .

701

702

703 704

705

706

707

708 709

710 711

712

713

714

715

716

717

718

719

720

721

722

723

724 725

726

727

728

729

730

731 732

733

734

735

736 737

738

739

740

741

742

743

744

745746

747

748749

750

4.2. Integration of ¹⁰Be-¹⁰B isotope systematics from this study with previous studies

In addition to the 25 ¹⁰Be–¹⁰B isochron regressions presented here, we are aware of 38 isochron regressions from previous studies (McKeegan et al., 2000; Sugiura et al., 2001; Marhas et al., 2002; MacPherson et al., 2003; Marhas and Goswami, 2003; Chaussidon et al., 2006; Liu et al., 2009; Liu et al., 2010; Wielandt et al., 2012; Gounelle et al., 2013; Srinivasan and Chaussidon, 2013; Liu and Keller, 2017; Sossi et al., 2017; Fukuda et al., 2019; Mishra and Marhas, 2019; Fukuda et al., 2021a). In order to properly evaluate and compare CAI data across studies, we reconstructed regressions in a consistent way with matrix matched standardization; in particular, in some cases (Wielandt et al., 2014), we corrected the data using more appropriate reported relative sensitivity factors (Fukuda et al., 2018; Dunham et al., 2020). The primary reason we reconstructed previously reported regressions is that some did not present the MSWD: because this value is used to evaluate the degree of over- or underdispersion of the data fit to a linear regression, it is essential to consider when determining the reliability and robustness of an isochron. We found that, of the 38 CAI regressions, 9 have $MSWD > 1+2\sigma_{MSWD}$, indicating they have < 5% probability of being an undisturbed isochron (Wendt and Carl, 1991). Although these CAIs likely contained live ¹⁰Be, the inferred ¹⁰Be/⁹Be ratios are unreliable because of the high MSWD, so we do not include these data in our overall interpretations. We note that some of the regressions only have a few data points that define the regression; in these cases, if only a single data point is off the regression line, the MSWD will likely be high. To process literature data consistently, we followed the MSWD < $1+2\sigma_{MSWD}$ criterion without weighting the number of data points per regression in interpreting the robustness of regressions. Of the nine CAI regressions with high MSWD, one is from a CH/CB, four are from CV3_{ox} chondrites, three are from CV3_{red} chondrites, and one is from a CO3 chondrite (see Supplementary Materials; regressions with high MSWD are indicated by 'X'). Five of these nine regressions show inferred ¹⁰Be/⁹Be ratios that are inconsistent with 10 Be/ 9 Be ~ (7–8) × 10⁻⁴, with three of these showing 10 Be/ 9 Be >>7 × 10⁻⁴.

As discussed in section 4.1, to determine if ¹⁰Be is distributed homogeneously in CAIs among the integrated dataset, we plotted the probability density of the combined data from this study and from the literature (only those ¹⁰Be/⁹Be values based on regressions with acceptable MSWD values for valid isochrons were used). Including the 25 isochron regressions from this study, a total of 54 CAI regressions are represented in Fig. 5. The data are predominantly distributed about a single peak at ${}^{10}\text{Be}/{}^{9}\text{Be} = 7.1 \times 10^{-4} \text{ (FWHM} = 3.1), however, there are$ smaller peaks at 3.1, 4.0, and 5.1 \times 10⁻⁴ (gray curve in Fig. 5). The three smaller peaks represent individual FUN CAIs and are distinguishable because data for these CAIs have unusually small uncertainties. We note that we only analyzed one FUN CAI while the literature data includes ¹⁰Be/⁹Be values from seven FUN CAI and PLAC isochron regressions. The n=54 probability density distribution indicates that the data belong to two groups: the small group of relatively few isotopically distinct FUN CAIs and PLACs, and the predominant group of normal CAIs. The probability density distribution shows three peaks for the FUN CAIs and PLACs indicating that in addition to being distinct from regular CAIs, with respect to ¹⁰Be, they are also distinct from each other. The data show that 87% of CAI isochron regressions center around ¹⁰Be/⁹Be $\sim 7.1 \times 10^{-4}$, the predominant probability density distribution peak. Three CAIs within this group (6%), though, have 10 Be/ 9 Be >> 7.1 × 10⁻⁴. The FUN CAIs and PLACs with 10 Be/ 9 Be \sim (3–5) × 10⁻⁴ reflect 13% of the total CAI isochron regressions (Fig. 4).

We also constructed a probability density distribution (blue curve in Fig. 5) with 47 CAI isochron regressions (from this study and the literature), but not including any FUN CAI or PLAC data. This distribution has the same peak as the gray curve in Fig. 5, at 10 Be/ 9 Be = 7.1×10^{-4} (FWHM = 2.4), but has no small peaks at 10 Be/ 9 Be < 7×10^{-4} . The 47 CAI regressions together have a weighted mean of 10 Be/ 9 Be = $(7.1 \pm 0.2) \times 10^{-4}$. Within this distribution, there are three CAIs with higher 10 Be/ 9 Be ratios that are not consistent with this value. They do not significantly affect the distribution or weighted mean because these regressions have large uncertainties. We discuss these data in more detail below (in section 4.3.3.). The probability density distributions shown in Fig. 5 suggest that while most CAIs recorded the same value of 10 Be/ 9 Be in the nebular environment in which they formed, there are some unusual CAIs that apparently recorded different 10 Be/ 9 Be ratios (FUN CAIs, PLACs, and three other CAIs with 10 Be/ 9 Be >> 7.1×10^{-4}).

4.3. Correlation of ¹⁰Be with ²⁶Al, oxygen isotopes, ⁵⁰Ti, and REEs

4.3.1. Importance of ²⁶Al-²⁶Mg, oxygen isotopes, ⁵⁰Ti, and REEs

To determine the origin of 10 Be, it is important to consider other isotopes measured in the same CAIs to constrain their formation and processing histories. We do not provide an indepth introduction or evaluation of each isotope system and CAI; instead, we focus on the implications of the additional information on our understanding of 10 Be in the early Solar System. We have compiled available isotopic information for all CAIs (from this and previous studies, including those with poor MSWD) for which 10 Be $^{-10}$ B isotope data have been determined, including the 26 Al $^{-26}$ Mg and oxygen isotopic data presented in this study, as well as ϵ^{50} Ti values and REE patterns, when available (Supplementary Materials).

The SLR ²⁶Al has been extensively utilized as a high-resolution chronometer for early Solar System events (i.e., Davis and McKeegan, 2014). We compare the inferred initial abundances of ²⁶Al and ¹⁰Be with the goals of: 1) understanding the relative age of a CAI; 2) determining if the CAI was extensively heated given that ²⁶Al–²⁶Mg can be reset in some or all minerals when a CAI is partially melted (i.e., Dauphas and Chaussidon, 2011); and 3) identifying ²⁶Al-poor CAIs (such as FUN CAIs).

Oxygen isotopes are key to classifying meteorites in general as well as CAIs. With regards to ¹⁰Be, we use oxygen isotopes to 1) identify FUN CAIs; and 2) determine how pristine the CAI is (i.e., a ¹⁶O-rich signature indicates that it is more pristine). We also utilize oxygen isotope compositions to better understand the oxygen isotope reservoirs that a CAI was exposed to during its formation and processing (e.g., Yurimoto et al., 2008).

Mass-independent Ti isotope anomalies in CAIs provide information about nucleosynthetic material incorporated into the solar nebula, nebular processing, and isotopic heterogeneity in the early Solar System (Williams et al., 2016; Kööp et al., 2016). For our purposes, we correlated ^{50}Ti to ^{10}Be in order to identify FUN CAIs; if the $\epsilon^{50}\text{Ti}$ value is high $(\epsilon^{50}\text{Ti}>\pm30)$, this is indicative of a FUN CAI or PLAC, as most normal CAIs have $\epsilon^{50}\text{Ti}\sim2-10$ (Trinquier et al., 2009; Williams et al., 2016; Davis et al., 2018; Render et al., 2019; Torrano et al., 2019).

The REE patterns in CAIs provide evidence for their condensation/evaporation origin or thermal processing. Most CAIs have unfractionated, flat REE patterns called group I patterns, that indicate that the CAI was condensed from a gas of solar composition. Fractionated group II patterns indicate that the CAI underwent a complex condensation/evaporation history, specifically, condensing from a gas that was depleted in an ultra-refractory component (Hu et al., 2021). Slightly fractionated group III patterns indicate

that the CAI experienced multiple heating/cooling events under changing redox conditions. Finally, some hibonite grains (i.e., HAL) have distinct REE patterns with negative Ce anomalies; this is interpreted to indicate that these hibonites formed by melt distillation under oxidizing conditions (MacPherson, 2014; Wang et al., 2001; Floss et al., 1996; Davis et al., 1982; Boynton, 1975). These formational and processing conditions are important to know when interpreting the initial ¹⁰Be abundance inferred in a CAI. In addition to REE patterns, ¹⁴⁹Sm–¹⁵⁰Sm isotope systematics can be used as an indicator of irradiation that occurred near the surface of the meteorite parent body; ¹⁴⁹Sm efficiently captures thermal neutrons, producing ¹⁵⁰Sm (Shollenberger et al., 2018). If a ¹⁵⁰Sm excess is discovered in a CAI, this is evidence that the CAI was close to the surface of the parent asteroid and therefore was irradiated by solar or galactic cosmic rays. In the context of ¹⁰Be, which is produced efficiently by irradiation, it is imperative to understand if the CAI experienced irradiation that could overprint the original ¹⁰Be signature.

4.3.2. ²⁶Al-²⁶Mg and oxygen isotope systematics in our CV3 and CR2 CAIs

From our CAI set measured for 10 Be $^{-10}$ B isotope systematics, we additionally measured 26 Al $^{-26}$ Mg isotope systematics in two CV3 and three CR2 CAIs and oxygen isotopes in five CV3 CAIs. CV3red CAIs *Agave* and *Cholla* and CR2 CAIs *Dalea*, *Creosote*, and *Yucca* all recorded canonical, or nearly canonical, 26 Al 27 Al ratios (Fig. 2) and are similar to other CV3 CAIs (Jacobsen et al., 2008) and CR2 CAIs (Makide et al., 2009). The mass-dependent Mg isotope composition (i.e., δ^{25} Mg; Supplemental Materials) is evidence that these samples were not extensively thermally processed. We note that the rim of CAI *Yucca* does appear to be reset; however, this is likely a later melting event or parent body processing that did not affect the CAI interior.

In our discussion of oxygen isotope compositions, we divide the CAIs based on their classification: 1 FTA, 1 CTA, 1 B1, and 2 B2s. The fine-grained fluffy type A (FTA) CAI, *Cholla*, is, for the most part, un-melted and has a ¹⁶O-rich signature. Only melilite in this CAI appears to have partially exchanged with a ¹⁶O-poor reservoir, potentially because the oxygen diffusion rate in melilite is the fastest (Ryerson and McKeegan, 1994). Other previously measured FTA CAIs have a similar oxygen isotope mineral variation except some have minerals with a larger range in Δ¹⁷O (Kawasaki et al., 2017; Park et al., 2012; Fagan et al., 2004). In addition, we note that there is a correlation between oxygen isotopes and melilite Åk content (¹⁶O-rich grains have more Al-rich melilite) as well as between oxygen isotopes and Ca-rich pyroxene Ti content (¹⁶O-rich grains have lower TiO₂). These correlations have been observed in other FTA CAIs and some type B CAIs (Kawasaki et al., 2018; Aléon, 2016; Katayama et al., 2012; Park et al., 2012) and may indicate that during melilite growth the surrounding oxygen environment shifted from ¹⁶O-poor to ¹⁶O-rich; this provides a hint that parent body alteration was not the main process affecting oxygen isotope distribution in CAI *Cholla*.

The CTA CAI studied in this work, B4 from NWA 6991, has ^{16}O -rich spinel and pyroxene but ^{16}O -poor melilite and anorthite. The ^{16}O -rich phases of B4 are on the mass-dependent fractionation trend, instead of the TFL. CTA CAIs studied previously have a range of oxygen isotope compositions with ^{16}O -rich spinel as well as melilite ranging to ^{16}O -poor compositions, but the $\Delta^{17}\text{O}$ ranges of the melilite and pyroxene are variable (Yurimoto et al., 2008). The type B2 CAIs discussed here (*Agave* and *Saguaro*) have ^{16}O -rich spinel and pyroxene, ^{16}O -poor melilite, and anorthite exhibiting a range in $\Delta^{17}\text{O}$. Although the type B1 CAI studied here has only a few measurements, it recorded ^{16}O -rich spinel and pyroxene, and ^{16}O -poor melilite and anorthite.

We find that B2 CAIs are slightly different than B1 CAIs with respect to oxygen isotopes. Type B2s are similar to B1s except they do not have a melilite mantle (so are less

melilite-rich; Bullock et al., 2013). Compared to earlier measurements of B1s (Kawasaki et al., 2018; Fagan et al., 2004), our B2 CAIs differ in that they contain anorthite with a large range in Δ^{17} O (consistent with Yurimoto et al., 2008). It has been hypothesized (Richter 2006; Mendybaev et al., 2006) that differing rates of molten CAI surface volatilization of Mg and Si during a melting event under reducing conditions could have caused the differences in Type B1s and B2s (Stolper and Paque, 1986). The different conditions under which the CTAs, Type B1s and Type B2s were formed and processed could have resulted in distinct oxygen isotope distributions in their minerals. Overall, the ²⁶Al–²⁶Mg and oxygen isotope data suggest that these CAIs are pristine, formed in a manner similar to most other CAIs, and were not significantly melted; they likely recorded the original ¹⁰Be signature in the nebula.

4.3.3. Two distinct CAI groups

 We have compiled available isotopic and geochemical data (from this study and previously reported literature data) that define 63 CAI 10 Be $^{-10}$ B isotope regressions (54 with MSWD values consistent with robust isochrons; Supplementary Materials). Considering these data, the CAIs for which the 54 robust regressions were obtained can be grouped into distinct isotopic populations, which has implications for constraining the origin of 10 Be. In the following discussion, we have included the number (n) of CAIs for which a particular isotopic or geochemical parameter was determined.

The main group of CAIs includes the vast majority (44 out of 54, or 81%) of the CAIs, which have ${}^{10}\text{Be}/{}^9\text{Be} \sim (7-8) \times 10^{-4}$, canonical ${}^{26}\text{Al}\,({}^{26}\text{Al}/{}^{27}\text{Al} \sim 5 \times 10^{-5},\,\text{n=}20)$, commonly ${}^{16}\text{Opor melilite}$ and anorthite but ${}^{16}\text{Opor melilite}$ and Ca-rich pyroxene (n=6), $\epsilon^{50}\text{Ti} \sim 2-10$ (n=5), and unfractionated group I REE patterns (n=4) (Podosek et al., 1991; Simon et al., 1994; Simon et al., 1999; Sugiura et al., 2001; MacPherson et al., 2003; Larsen et al., 2011; Wielandt et al., 2012; Srinivasan and Chaussidon, 2013; Render et al., 2019; Torrano et al., 2019; Hertwig et al., 2021).

The FUN CAIs and PLACs (n=7), which typically record low 10 Be/ 9 Be $\sim (3-5) \times 10^{-4}$ (Marhas et al., 2002; MacPherson et al., 2003; Marhas and Goswami, 2003; Liu et al., 2009; Liu et al., 2010; Wielandt et al., 2012; Tatischeff et al., 2014; Liu and Keller, 2017), also have low $^{26}\text{Al}/^{27}\text{Al} < 2 \times 10^{-5}$ (n=7), distinctively fractionated oxygen isotopes (n=4), anomalous ε^{50} Ti (n=3), and group II, III, or distillation REE patterns (n=4) (Fahey et al., 1987; Srinivasan et al., 2000; Thrane et al., 2008; Liu et al., 2009; Williams et al., 2017). Fractionated CAIs have experienced extensive mass-fractionation due to evaporation, which potentially disturbed the ¹⁰Be−¹⁰B systematics in a way that lowered the inferred initial ¹⁰Be/⁹Be, as discussed in section 4.1. Some other possibilities to explain the low ¹⁰Be/⁹Be ratio of FUN CAIs include that they recorded a heterogeneous nebula containing low ¹⁰Be/⁹Be regions, or that they recorded the ¹⁰Be/⁹Be of a spatially homogeneous solar nebula, but after significant decay of ¹⁰Be. Unlike FUN CAIs, some PLACs did not experience intense evaporation (most do not show fractionations in Ca and Ti; Kööp et al., 2018), so some of the discussed possibilities causing low ¹⁰Be/⁹Be values may not be applicable to PLACs. The time and place of formation of these CAIs is not as well understood as the time and place of formation of the main group of normal CAIs, and FUN CAIs saw additional physical processes that normal CAIs did not. These uncertainties complicate their interpretation.

There are 3 CAIs with high 10 Be/ 9 Be > 20×10^{-4} that do not fit into these two groups: *Lisa*, *Y20-1X1*, and *SA301*. CAI *Lisa* has an unfractionated group I REE pattern as well as elevated 150 Sm (Shollenberger et al., 2018). As discussed by Dunham et al. (2020), this is evidence that *Lisa* was located near the surface of the asteroid and received an extra dose of irradiation that produced spallogenic B, overprinting its original 10 Be- 10 B signature (Fig. 7). For reasonable solar energetic particle fluences as inferred from the neutron fluence constrained by the 150 Sm excess, *Lisa* is consistent with forming with the same initial 10 Be/ 9 Be

as CAIs in the main group (Fig. 7). CAI *Lisa* has clearly been disturbed, and the simplest explanation is that *Lisa* does not reflect the ¹⁰Be/⁹Be ratio of the time and place it formed. CAI *B4* from the same meteorite NWA 6991 also has high ¹⁵⁰Sm but a more common ¹⁰Be/⁹Be ratio; this is not necessarily inconsistent with the spatial variations of ¹⁵⁰Sm and spallogenic boron (Dunham et al., 2020).

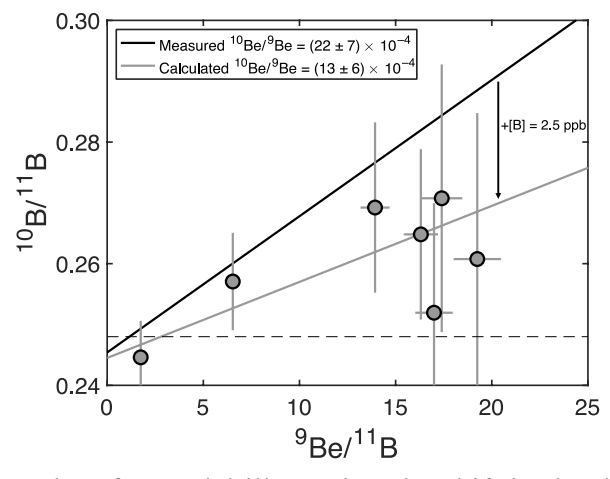


Fig. 7. Plot showing the results of a model illustrating the shift in the data for the CAI *Lisa* after addition of spallogenic B (suggested to be a consequence of cosmic ray exposure resulting in neutron irradiation on a parent body surface). The black line indicates the 10 Be $^{-10}$ B isochron for CAI *Lisa* based on its measured data (MSWD = 1.1); we have not shown the data points here for clarity. By adding 2.5 ppb of spallogenic B (with 10 B/ 11 B = 0.44) to each data point, we find that the resulting hypothetical data define a slope that is significantly lower (gray line and data points) with MSWD = 1.2. This figure is modified from Dunham et al. (2020).

Of the two other anomalous CAIs, CAI Y20-IXI has canonical 26 Al/ 27 Al and a fractionated group II pattern, indicating that it condensed from a gas formed by evaporation (Hu et al., 2021). CAI SA30I is 26 Al-poor and from the CH parent body. Additionally, these two CAIs include spots with some of the lowest boron concentrations in the datasets, down to $[B] \sim 5$ ng/g (Fukuda et al., 2019, 2021a). It will be necessary to find and study additional CAIs with high 10 Be/ 9 Be values to further constrain the origin of this poorly defined set of CAIs.

There are two CAIs, 31-2 and CH-C4, that fit into the main group of CAIs with 10 Be/ 9 Be $\sim 7.1 \times 10^{-4}$, but their other isotopic signatures are distinct. The UN CAI 31-2, which has 10 Be/ 9 Be = $(14.6 \pm 6.6) \times 10^{-4}$, is 26 Al-poor, and 16 O-rich (Simon et al., 2019b; Simon et al., 2019a). The hibonite CAI CH-C4 has 10 Be/ 9 Be = $(8.0 \pm 3.3) \times 10^{-4}$, is 26 Al-poor, has mass fractionated O isotopes, anomalous ε^{50} Ti, and a group III REE pattern (Marhas et al. 2003). The reason that these two unusual hibonite-rich CAIs recorded the 10 Be/ 9 Be ratios of normal CAIs remains unclear.

In summary, 44 of 54 CAIs with robust ${}^{10}\text{Be}{}^{-10}\text{B}$ isochrons appear to be in the main group with ${}^{10}\text{Be}/{}^9\text{Be} \sim 7.1 \times 10^{-4}$. Only 10 CAIs have inferred ${}^{10}\text{Be}/{}^9\text{Be}$ outside this range. Seven of these (five of which are FUN CAIs and two are PLACs) have lower values; these likely formed at a different time than normal CAIs and are strongly associated with mass-dependent fractionation likely caused by evaporation or distillation events. It remains to be confirmed if apparently lower ${}^{10}\text{Be}/{}^9\text{Be}$ values were generated by such events. Three have higher values, but one, Lisa, cannot be interpreted as evidence of a higher ${}^{10}\text{Be}/{}^9\text{Be}$ in the time and place it formed, because it was disturbed to some degree by a spallogenic overprint. The CAIs Y20-1XI and SA30I might provide evidence of heterogeneity of ${}^{10}\text{Be}$ in the solar nebula. At least 81% of CAIs record a ${}^{10}\text{Be}/{}^9\text{Be}$ ratio consistent with $\sim 7.1 \times 10^{-4}$. Therefore, the

preponderance of evidence is that the ¹⁰Be/⁹Be ratio in the solar nebula was largely uniform, but that some CAIs may record different values due to their distinctive histories.

5. On the origin of ¹⁰Be and astrophysical implications.

942 943 944

945

946 947

948

949 950

951

952

953

954

955956

957

958

959 960

961

962

963 964

965

966

967 968

969

970

971

972

973

974

975

976

977

978 979

980

981

982

983

984 985

986

987

988

939

940

941

We can compare the distribution of ¹⁰Be in CAIs to the distribution predicted by the models to infer the most likely origin of ¹⁰Be. The two end-member scenarios are that ¹⁰Be was produced either by GCR irradiation in the molecular cloud and inherited into the solar nebula or by solar energetic particle (SEP) irradiation of gas and/or solids in the solar nebula. The hybrid scenario between these end-members would be that some ¹⁰Be was inherited from the molecular cloud and then irradiation in the nebular contributed the remaining ¹⁰Be. So, which of these scenarios best describes the data?

As stated in the introduction, we used models (Jacquet, 2019; Yang and Ciesla, 2012) to predict that for nebular irradiation, a significant fraction (> ~50%) of CAIs would record 10 Be/ 9 Be values greater than in most CAIs (exceeding the mean by at least 2σ), assuming that CAIs did not form at the same time and place. Specifically, if the mean 10 Be/ 9 Be ratio $\sim 7.1 \times 10^{-10}$ 10^{-4} in all CAIs that were formed or thermally processed by t < 0.3 Ma, as found in this study, CAIs formed or processed at t > 0.3 Ma are estimated to record values of $(6-21) \times 10^{-4}$; > 50%of CAIs would have ${}^{10}\text{Be}/{}^{9}\text{Be} < 5 \times 10^{-4} \text{ or} > 10 \times 10^{-4}$. However, if more than 50% of CAIs record 10 Be/ 9 Be values consistent with the mean of $\sim 7.1 \times 10^{-4}$, inheritance from the molecular cloud would have likely contributed significantly to the ¹⁰Be inventory of the solar nebula. The hybrid scenario, where approximately half of ¹⁰Be is produced by irradiation, we estimate that >25% of CAIs may still be expected to record ¹⁰Be/⁹Be values greater than the mean. Based on all available data, we find that 81% of robust CAI isochron regressions record the mean 10 Be/ 9 Be ~ 7.1 × 10⁻⁴, 13% record 10 Be/ 9 Be resolvably lower than this mean value and 6% record higher. Because the fraction of CAIs that record values (within their uncertainties) of the mean far exceeds 50%, we suggest that the end-member scenario of irradiation in the nebula is unlikely to have been the predominant producer of ¹⁰Be found in CAIs. However, given that 19% of CAIs record values resolvably distinct from the mean, it implies that even if ¹⁰Be was mostly inherited from the molecular cloud, some fraction may indeed still have been produced by local irradiation.

If all the ¹⁰Be was inherited from the molecular cloud, it is not clear what process(es) the apparent variations in the inferred ¹⁰Be/⁹Be reflect. We cannot rule out entirely that some variations are due to SEP irradiation of the nebula, affecting the gas which the CAIs formed from, or affecting the CAIs themselves by in situ irradiation. However, in correlating ¹⁰Be abundance with other isotopic and elemental evidence, some additional possibilities arise to explain the ¹⁰Be/⁹Be ratios distinct from the mean recorded by CAIs. The first possibility is timing. Most CAIs with relatively low or high ¹⁰Be/⁹Be ratios also show non-canonical initial ²⁶Al; formation at $t \sim 1$ Ma in a disk with an initial 10 Be/ 9 Be $\sim 7.1 \times 10^{-4}$ would yield 10 Be/ 9 Be = 4×10^{-4} . This scenario is typically not favored (Krot, 2019), however it is still a possibility. Another possibility is secondary processing of CAIs or their precursor materials, which can be evidenced by reset ²⁶Al-²⁶Mg isotope systematics, isotope anomalies, or CAIs from the CH/CB parent body. As suggested in section 4.1, FUN CAIs likely experienced evaporation, as is evidenced by their mass-dependent isotope fractionations, which may also have affected ¹⁰Be– ¹⁰B isotope systematics. It is possible that the CH/CB parent body, which underwent a highenergy collision event, could have introduced conditions to alter initial CAI ¹⁰Be/⁹Be ratios; an impact plume from the irradiated surface of a CH/CB parent body precursor could have mixed with the original CAI and chondrule material. CH CAI SA301 has low ²⁶Al and could have been altered by the impact plume; however, oxygen isotopes and other chemical and isotopic measurements are necessary to confirm this. The FUN CAIs, PLACs, and CO3 CAI Y20-1X1

from the combined dataset show group II, III, and distillation REE patterns. We did not measure a CAI with a group II pattern, so cannot confirm a possible correlation between initial 10 Be/ 9 Be ratios and group II REE patterns (Fukuda et al., 2021a). These are speculative ideas that need to be tested, but the larger point is that unusual CAIs with isotopic anomalies, low 26 Al, or evidence of additional processing (such as formation on the CH/CB parent body and/or the presence of group II REE patterns), are the only ones that show 10 Be/ 9 Be values distinct from those of normal CAIs that have 10 Be/ 9 Be $\sim 7.1 \times 10^{-4}$. Whether these distinct 10 Be/ 9 Be values are due to nebular irradiation, or another process, is unclear.

We favor inheritance because we interpret that CAIs with 10 Be/ 9 Be ratios resolvable above or below the mean value did not record the 10 Be signature in the times and places of regular CAI formation. However, we acknowledge that the hybrid scenario is a possibility because the predicted model fractions are estimates. More quantitative and predictive models for the origin of 10 Be are necessary to resolve this. Whether all the 10 Be inferred to be present in CAIs was inherited from the molecular cloud or just most of it, many of the astrophysical implications are the same. Either ratio of potentially inherited material, 10 Be/ 9 Be $\approx 5 \times 10^{-4}$, or $(7-8) \times 10^{-4}$, is significantly higher than the 10 Be/ 9 Be ratio ($\approx 1 \times 10^{-4}$; Tatischeff et al., 2014) predicted to result from spallation of molecular cloud material by present-day Galactic cosmic ray (GCR) fluxes. To explain the inherited 10 Be/ 9 Be = $(5 \text{ to } 8) \times 10^{-4}$, an increase in the GCR flux in the Sun's molecular cloud above present-day background levels seems to be required. In future work, we will investigate whether this scenario is quantitatively likely.

5. CONCLUSIONS

We measured the ¹⁰Be–¹⁰B isotope systematics in 29 CAIs from CV3, CO3, CR2, and CH/CB chondrites, based upon which we reported 25 isochron regressions. For a subset of these CAIs, we also measured ²⁶Al-²⁶Mg isotope systematics and oxygen isotope compositions. The 25 CAI isochron regressions form a single probability density function peak at 10 Be/ 9 Be = 7.4×10^{-4} , suggesting that the 10 Be distribution in the CAI forming region was homogeneous (although the FUN CAI measured in this study records a ¹⁰Be/⁹Be ratio lower than this peak value). We then integrated our CAI data with previously reported data for other CAIs and find that 54 robust ¹⁰Be-¹⁰B isochron regressions yield ¹⁰Be/⁹Be values that are distributed about a probability density peak at ${}^{10}\text{Be}/{}^{9}\text{Be} = 7.1 \times 10^{-4}$. The 7 CAI isochron regressions with inferred ¹⁰Be/⁹Be ratios below this value are FUN CAIs or PLACs with 10 Be/ 9 Be $\sim (3-5) \times 10^{-4}$. Three of the CAI isochron regressions recorded higher 10 Be/ 9 Be > 20 \times 10⁻⁴. To better understand these groups of CAIs, we correlated inferred 10 Be/ 9 Be ratios with other elemental and isotopic parameters, such as ²⁶Al-²⁶Mg systematics, oxygen isotope compositions, ε^{50} Ti values, and REE concentrations. The main group of CAIs (81%) record 10 Be/ 9 Be ~ 7.1 × 10⁻⁴, canonical 26 Al/ 27 Al, typical oxygen isotope compositions ranging from $\Delta^{17}O = -1\%$ to -25%, $\epsilon^{50}Ti \sim 2-10$, and group I REE patterns. The FUN CAI and PLAC group (13%) recorded low 10 Be/ 9 Be ~ (3–5) × 10⁻⁴, low 26 Al/ 27 Al, fractionated oxygen isotopes, large ε^{50} Ti anomalies, group II, III and distilled REE patterns. The three CAIs having high 10 Be/ 9 Be $> 20 \times 10^{-4}$ have varied isotopic and elemental systematics: *Lisa* with high ¹⁴⁹Sm indicating that it was irradiated on the parent body, ²⁶Al-poor CAI SA301 from a CH chondrite, and Y20-1X1 with canonical ²⁶Al/²⁷Al and a group II REE pattern. These characteristics elucidate that unusual CAIs, those with low ²⁶Al/²⁷Al, mass fractionated oxygen isotopes, large ⁵⁰Ti anomalies, or non-group I REE patterns, tend to have ¹⁰Be/⁹Be lower or higher than the normal group of CAIs. Because FUN CAIs and PLACs are a clearly distinct group, we calculate the weighted mean of the remaining 47 CAI isochron regressions to be $^{10}\text{Be}/^{9}\text{Be} = (7.1 \pm 0.2) \times$ 10^{-4} .

To interpret these data with the goal of constraining the origin of 10 Be, we used literature models to predict that if 10 Be was formed in the molecular cloud and inherited into our Solar System, all CAIs that formed at the beginning of the Solar System (i.e., t=0) should have recorded the same 10 Be/ 9 Be ratio; and if 10 Be was formed by SEP irradiation in the solar nebula, $\sim 50\%$ of CAIs would record 10 Be/ 9 Be values resolvably lower or higher than the CAI average. Because 81% of CAIs record a 10 Be/ 9 Be ratio consistent with $\sim 7.1 \times 10^{-4}$, they provide evidence that 10 Be was predominantly inherited into the solar nebula from the molecular cloud. Because 100% of CAIs do not have the same 10 Be/ 9 Be, further studies will be required to understand the origins of these differing values. Irradiation of disk material by SEPs is a possibility, but it is also possible that FUN CAIs have low 10 Be/ 9 Be due to B loss during evaporation or because they formed after normal CAIs. These possibilities complicate the interpretation that CAIs with 10 Be/ 9 Be distinct from $\sim 7.1 \times 10^{-4}$ recorded 10 Be formed by irradiation in the nebula. Regardless of the cause of these few variations, we conclude that the overall preponderance of uniform initial 10 Be/ 9 Be strongly suggests that Solar System 10 Be was predominantly inherited from the molecular cloud.

ACKNOWLEDGEMENTS

We are grateful to Dr. Lynda Williams for her assistance in the ASU SIMS lab. We thank Dr. Ryan Ogliore and Dr. Chris Coath for useful discussions about statistics and ratio determination. We acknowledge the use of facilities within the Eyring Materials Center at ASU, supported in part by NNCI-ECCS-1542160, with the assistance of Dr. Axel Wittmann. We acknowledge ASU's Buseck Center for Meteorite Studies collection for providing samples of NWA 5028, NWA 6991 CAI B4, Leoville, Allende CAI CMS-1, NWA 7891, and NWA 7892; the Field Museum of Natural History for Allende CAIs TS23A and TS68; Dr. Gregory Brennecka for providing samples of DaG 005 and DaG 027; Dr. Devin Schrader for providing sample Shisr 033, and the US Antarctic meteorite collection for samples of DOM 08006, MIL 090657, and LAP 02342. US Antarctic meteorite samples are recovered by the Antarctic Search for Meteorites (ANSMET) program, which has been funded by NSF and NASA, and characterized and curated by the Department of Mineral Sciences of the Smithsonian Institution and the Astromaterials Acquisition and Curation Office at NASA Johnson Space Center. We acknowledge some prominent women astronauts and researchers in astronomy, geology, and physics by naming the CO3 and CH/CB CAIs studied here after them (Goeppert, Jemison, Anning, Mitchell, Bascom, Krafft, Burnell, Meitner, Rubin, Tharp, and Tereshkova); these women's achievements and contributions to science remain largely unacknowledged, and they are deserving of greater recognition. This work is supported by the NASA Earth and Space Sciences Fellowship grant NNX1AP48H (ETD and MW), 51 Pegasi b grant #2020-1829 (ETD), grants NNX15AH41G (MW), NNX17AI43G (SS), and 80NSSC18K0602 (ML) from the NASA Emerging Worlds program. The results reported herein benefitted from collaborations and/or information exchange within NASA's Nexus for Exoplanet System Science (NExSS) research coordination network sponsored by NASA's Science Mission Directorate; we gratefully acknowledge support from NExSS grant NNX15AD53G (SJD). The UCLA ion microprobe facility is partially supported by a grant from the NSF Instrumentation and Facilities program (EAR-1734856; ML), as is the ASU secondary ion mass spectrometer (NSF EAR 1819550; RLH). WiscSIMS is partly supported by NSF (EAR-1658823; NK).

1088 APPENDIX A. SUPPLEMENTARY MATERIAL

1089

1090 Supplementary data associated with this article can be found, in the online version, at:

1091

- 1092 Supplementary files include:
- Re-classification of NWA 5028, NWA 7891, and NWA 5508 1093
- 1094 CAI images including mineralogy and SIMS pit labels
- 1095 Correlated isotopes of 63 CAIs
- 1096 Beryllium-10 isotope systematic raw and corrected data
- 1097 Aluminum-26 isotope systematic raw and corrected data
- 1098 Oxygen isotope systematic raw and corrected data

1099 1100

REFERENCES

1101

1108

1109

1110

- 1102 Aléon J. (2016) Oxygen isotopes in the early protoplanetary disk inferred from pyroxene in a classical type B CAI. Earth Planet. Sci. Lett. 440, 62–70. 1103
- 1104 Baker, D.R. (1992) Tracer diffusion of network formers and multicomponent diffusion 1105 in dacitic and rhyolitic melts. Geochimica et Cosmochimica Acta, 56, 617–631.
- Boynton W. V. (1975) Fractionation in the solar nebula: condensation of vttrium and the rare 1106 1107 earth elements. Geochim. Cosmochim. Acta 39, 569-584.
 - Brennecka G. A., Burkhardt C., Budde G., Kruijer T. S., Nimmo F. and Kleine T. (2020) Astronomical Context of Solar System formation for molybdenum isotopes in meteorite inclusions. **840**, 837–840.
- Bullock E. S., Knight K. B., Richter F. M., Kita N. T., Ushikubo T., MacPherson G. J., Davis 1111 1112 A. M. and Mendybaev R. A. (2013) Mg and Si isotopic fractionation patterns in types B1 1113 and B2 CAIs: Implications for formation under different nebular conditions. Meteorit. 1114 Planet. Sci. 48, 1440-1458.
- 1115 Chakraborty, S., Dingwell, D.B., and Chaussidon, M. (1993) Chemical diffusivity of boron in 1116 melts of haplogranitic composition. Geochimica et Cosmochimica Acta, 57, 1741–1751
- 1117 Chaussidon M., Robert F. and McKeegan K. D. (2006) Li and B isotopic variations in an Allende CAI: Evidence for the in situ decay of short-lived ¹⁰Be and for the possible 1118 1119 presence of the short-lived nuclide ⁷Be in the early solar system. Geochemica 1120 Cosmochem. Acta 70, 224–245.
- Chmeleff J., von Blanckenburg F., Kossert K. and Jakob D. (2010) Determination of the 10Be 1121 1122 half-life by multicollector ICP-MS and liquid scintillation counting. Nucl. Instruments 1123 Methods Phys. Res. Sect. B Beam Interact. with Mater. Atoms 268, 192–199.
- 1124 Coath C. D., Steele R. C. J. and Lunnon W. F. (2013) Statistical bias in isotope ratios. J. Anal. At. Spectrom. 28, 52-58. 1125
- 1126 Connelly J. D., Bizzzaro M., Krot A. N., Nordlund A., Wielandt D., and Ivanova M. (2012) 1127 The absolute chronology and thermal processing of solids in the solar protoplanetary disk. 1128 Science 338, 651-655.
- 1129 Dauphas N. and Chaussidon M. (2011) A Perspective from Extinct Radionuclides on a Young 1130 Stellar Object: The Sun and Its Accretion Disk. Annu. Rev. Earth Planet. Sci. 39, 351-1131 386.
- 1132 Davidson J., Alexander C. M. O'D., Stroud R. M., Busemann H. and Nittler L. R. (2019a) Mineralogy and petrology of Dominion Range 08006: A very primitive CO3 1133 1134 carbonaceous chondrite. Geochim. Cosmochim. Acta 265, 259-278.
- 1135 Davidson J., Schrader D. L., Alexander C. M. O'D., Nittler L. R. and Bowden R. (2019b) Reexamining thermal metamorphism of the Renazzo-like (CR) carbonaceous chondrites: 1136
- 1137 Insights from pristine Miller Range 090657 and shock-heated Graves Nunataks 06100.

- 1138 *Geochim. Cosmochim. Acta* **267**, 240–256.
- Davis A. M. and McKeegan K. D. (2014) Short-Lived Radionuclides and Early Solar System
 Chronology. In *Treatise on Geochemistry* (eds. E. Eds., H. D. Holland, and K. K.
 Turekian). Elsevier, Oxford. pp. 361–395.
- Davis A. M., Richter F. M., Mendybaev R. A., Janney P. E., Wadhwa M. and McKeegan K. D. (2015) Isotopic mass fractionation laws for magnesium and their effects on ²⁶Al-²⁶Mg systematics in solar system materials. *Geochim. Cosmochim. Acta* **158**, 245–261.
- Davis A. M., Tanaka T., Grossman L., Lee T. and Wasserburg G. J. (1982) Chemical composition of HAL, an isotopically-unusual Allende inclusion. *Geochim. Cosmochim. Acta* **46**, 1627–1651.
- Davis A. M., Zhang J., Greber N. D., Hu J., Tissot F. L. H. and Dauphas N. (2018) Titanium isotopes and rare earth patterns in CAIs: Evidence for thermal processing and gas-dust decoupling in the protoplanetary disk. *Geochim. Cosmochim. Acta* 221, 275–295.
- Desch S. J., Connolly, Jr. H. C. and Srinivasan G. (2004) An interstellar origin for the beryllium-10 in calcium-rich, aluminum-rich inclusions. *Astrophys. J.* **602**, 528–542.
- Dunham E. T., Wadhwa M., Desch S. J. and Hervig R. L. (2020) Best practices for determination of initial ¹⁰Be/⁹Be in early Solar System materials by SIMS. *Geostand. Geoanalytical Res.* **12329**.
- Fagan T. J., Krot A. N., Keil K. and Yurimoto H. (2004) Oxygen isotopic alteration in Ca-Alrich inclusions from Efremovka: Nebular or parent body setting? *Meteorit. Planet. Sci.* **39**, 1257–1272.
- Fahey A. J., Goswami J. N., McKeegan K. D. and Zinner E. (1987) ²⁶Al, ²⁴⁴Pu, ⁵⁰Ti, REE, and trace element abundances in hibonite grains from CM and CV meteorites. *Geochim.* 1161 *Cosmochim. Acta* **51**, 329–350.
- Floss C., El Goresy A., Zinner E., Kransel G., Rammensee W. and Palme H. (1996) Elemental and isotopic fractionations produced through evaporation of the Allende CV chondrite: Implications for the origin of HAL-type hibonite inclusions. *Geochim. Cosmochim. Acta* **60**, 1975–1997.
- Fukuda K., Beard B. L., Dunlap D. R., Spicuzza M. J., Fournelle J. H., Wadhwa M. and Kita N. T. (2020) Magnesium isotope analysis of olivine and pyroxene by SIMS: Evaluation of matrix effects. *Chem. Geol.* **540**, 119482.
- Fukuda K., Brownlee D. E., Joswiak D. J., Tenner T. J., Kimura M. and Kita N. T. (2021b)
 Correlated isotopic and chemical evidence for condensation origins of olivine in comet
 81P/Wild 2 and in AOAs from CV and CO chondrites. *Geochim. Cosmochim. Acta* 293,
 544–574.
- Fukuda K., Fuijya W., Hiyagon H., Makino Y., Sugiura N., Takahata N., Hirata T. and Sano Y. (2018) Beryllium-boron relative sensitivity factors for melilitic glasses measured with a NanoSIMS ion microprobe. *Geochem. J.* **52**, 255–262.
- Fukuda K., Hiyagon H., Fujiya W. and Kagoshima T. (2021a) Irradiation origin of ¹⁰Be in the solar nebula: Evidence from Li-Be-B and Al-Mg isotope systematics, and REE abundances of CAIs from Yamato-81020 CO3.05 chondrite. *Geochim. Cosmochim. Acta* **293**, 187–204.
- Fukuda K., Hiyagon H., Fujiya W., Takahata N., Kagoshima T. and Sano Y. (2019) Origin of the short-lived radionuclide ¹⁰Be and its implications for the astronomical setting of CAI formation in the solar protoplanetary disk. *Astrophys. J.* **886**, 34–45.
- Galy A., Yoffe O., Janney P. E., Williams R. W., Cloquet C., Alard O., Halicz L., Wadhwa M., Hutcheon I. D., Ramon E. and Carignan J. (2003) Magnesium isotope heterogeneity of the isotopic standard SRM980 and new reference materials for magnesium-isotoperatio measurements. *J. Anal. At. Spectrom.* **18**, 1352–1356.
- Gounelle M., Chaussidon M. and Rollion-Bard C. (2013) Variable and extreme irradiation

- 1188 conditions in the early solar system inferred from the initial abundance of ¹⁰Be in Isheyevo CAIs. *Astrophys. J.* **763**, L33.
- Gounelle M., Shu F. H., Shang H., Glassgold A. E., Rehm K. E. and Lee T. (2001) Extinct radioactivities and protosolar cosmic rays: self-shielding and light elements. *Astrophys. J.* **548**, 1051–1070.
- Gounelle M., Shu F. H., Shang H., Glassgold A. E., Rehm K. E. and Lee T. (2006) The Irradiation Origin of Beryllium Radioisotopes and Other Short-lived Radionuclides. *Astrophys. J.* **640**, 1163–1170.
- Heck P., Gyngard F., Ott U., Meier M., Vila J. N., Amari S., Zinner E., Lewis R. S., Baur H. and Wieler R. (2009) Interstellar residence times of presolar SiC dust grains from the murchison carbonaceous meteorite. *Astrophys. J.* **698**, 1155–1164.
- Hertwig A. T., Kimura M., Ushikubo T., Defouilloy C. and Kita N. T. (2019) The ²⁶Al-²⁶Mg systematics of FeO-rich chondrules from Acfer 094: Two chondrule generations distinct in age and oxygen isotope ratios. *Geochemica Cosmochem. Acta* **253**, 111–126.
- Hertwig A. T., Liu M.-C., Brearley A. J. and Simon S. B. (2021) Petrographic and isotopic investigations of two unusual Ca-Al-rich inclusions from primitive CO3 chondrites. *Geochim. Cosmochim. Acta* **296**, 75–96.
- Hervig R. L., Moore G. M., Williams L. B., Peacock S. M., Holloway J., and Roggensack K. (2002) Isotopic and elemental partitioning of boron between hydrous fluid and silicate melt. *American Mineralogist* **87** 769-774.
- Hu J. Y., Dauphas N., Tissot F. L. H., Yokochi R., Ireland T. J., Zhang Z., Davis A. M., Ciesla F. J., Grossman L., Charlier B. L. A., Roskosz M., Alp E. E., Hu M. Y. and Zhao J. (2021) Heating events in the nascent solar system recorded by rare earth element isotopic fractionation in refractory inclusions. *Sci. Adv.* 7, 22–28.
- Jacobsen B., Yin Q., Moynier F., Amelin Y., Krot A. N., Nagashima K., Hutcheon I. D. and Palme H. (2008) ²⁶Al-²⁶Mg and ²⁰⁷Pb-²⁰⁶Pb systematics of Allende CAIs: Canonical solar initial ²⁶Al/²⁷Al ratio reinstated. *Earth Planet. Sci. Lett.* **272**, 353–364.
- Jacquet E. (2019) On beryllium-10 production in gaseous protoplanetary disks and implications on the astrophysical setting of refractory inclusions. *Astron. Astrophys.* **624**, A131.
- Katayama J., Itoh S. and Yurimoto H. (2012) Oxygen isotopic zoning of reversely zoned melilite crystals in a fluffy type A Ca-Al-rich inclusions from the Vigarano meteorite. **2106**, 2094–2106.
- 1220 Kawasaki N., Park C., Sakamoto N., Park S. Y., Kim H. Y., Kuroda M, and Yurimoto H. (2019)
 1221 Variations in initial 26Al/27Al ratios among fluffy type A Ca-Al-rich inclusions from
 1222 reduced CV chondrites *Earth Planet. Sci. Lett.* **511**, 25–35.
- Kawasaki N., Itoh S., Sakamoto N. and Yurimoto H. (2017) Chronological study of oxygen isotope composition for the solar protoplanetary disk recorded in a fluffy Type A CAI from Vigarano. *Geochim. Cosmochim. Acta* **201**, 83–102.
- Kawasaki N., Simon S. B., Grossman L., Sakamoto N. and Yurimoto H. (2018) Crystal growth and disequilibrium distribution of oxygen isotopes in an igneous Ca-Al-rich inclusion from the Allende carbonaceous chondrite. *Geochim. Cosmochim. Acta* **221**, 318–341.
- Kita N. T., Nagahara H., Tachibana S., Tomomura S., Spicuzza M. J., Fournelle J. H. and Valley J. W. (2010) High precision SIMS oxygen three isotope study of chondrules in LL3 chondrites: Role of ambient gas during chondrule formation. *Geochim. Cosmochim. Acta* 74, 6610–6635.
- Kita N. T., Ushikubo T., Knight K. B., Mendybaev R. A., Davis A. M., Richter F. M. and Fournelle J. H. (2012) Internal ²⁶Al–²⁶Mg isotope systematics of a Type B CAI: Remelting of refractory precursor solids. *Geochim. Cosmochim. Acta* **86**, 37–51.
- Kita N. T., Yin Q., MacPherson G. J., Ushikubo T., Jacobsen B., Nagashima K., Kurahashi E., Krot A. N. and Jacobsen S. B. (2013) Al-Mg isotope systematics of the first solids in the

- early solar system. *Meteorit. Planet. Sci.* **48**, 1383–1400.
- Kööp L., Nakashima D., Heck P. R., Kita N. T., Tenner T. J., Krot A. N., Nagashima K., Park C., and Davis A. M., (2016) New constraints on the relationship between ²⁶Al and oxygen, calcium, and titanium isotopic variation in the early Solar System from a multielement isotopic study of spinel-hibonite inclusions. *Geochim. Cosmochim. Acta* **184**, 151–172.
- 1243 Kööp L., Davis A. M., Krot A. N., Nagashima K. and Simon S. B. (2018) Calcium and titanium 1244 isotopes in refractory inclusions from CM, CO, and CR chondrites. *Earth Planet. Sci. Lett.* 1245 **489**, 179–190.
- Korschinek G., Bergmaier A., Faestermann T., Gerstmann U. C., Knie K., Rugel G., Wallner A., Dillmann I., Dollinger G., von Gostomski C. L., Kossert K., Maiti M., Poutivtsev M. and Remmert A. (2010) A new value for the half-life of ¹⁰Be by Heavy-Ion Elastic Recoil Detection and liquid scintillation counting. *Nucl. Instruments Methods Phys. Res. Sect. B Beam Interact. with Mater. Atoms* **268**, 187–191.
- Krot A. N. (2019) Refractory inclusions in carbonaceous chondrites: Records of early solar system processes. *Meteorit. Planet. Sci.* **54**, 1647–1691.
- 1253 Krot A. N., Nagashima K., Bizzarro M., Huss G. R., Davis A. M., Meyer B. S. and Ulyanov 1254 A. A. (2008) Multiple generations of refractory inclusions in the metal-rich carbonaceous 1255 chondrites Acfer 182/214 and Isheyevo. *Astrophys. J.* **672**, 713–721.
- 1256 Krot A. N., Nagashima K., Lyons J. R., Lee J. E. and Bizzarro M. (2020) Oxygen isotopic 1257 heterogeneity in the early Solar System inherited from the protosolar molecular cloud. *Sci.* 1258 *Adv.* **6**, 1–8.
- Krot A. N., Nagashima K., Wasserburg G. J., Huss G. R., Papanastassiou D., Davis A. M., Hutcheon I. D. and Bizzarro M. (2014) Calcium-aluminum-rich inclusions with fractionation and unknown nuclear effects (FUN CAIs): I. Mineralogy, petrology, and oxygen isotopic compositions. *Geochim. Cosmochim. Acta* 145, 206–247.
- 1263 Krot A. N., Peaev M., Scott E., Choi B.-G., Zolensky M. and Keil K. (1998) Progresive 1264 alteration in CV3 chondrites: more evidence for asteroidal alteration. *Meteorit. Planet.* 1265 *Sci.* **1085**, 1065–1085.
- Larsen K. K., Trinquier A., Paton C., Schiller M., Wielandt D., Ivanova M. A., Connelly J. N.,
 Nordlund Å., Krot A. N. and Bizzarro M. (2011) Evidence for Magnesium Isotope
 Heterogeneity in the Solar Protoplanetary Disk. *Astrophys. J.* 735, L37.
- Liu M.-C., Han J., Brearley A. J. and Hertwig A. T. (2019) Aluminum-26 chronology of dust coagulation and early solar system evolution. *Sci. Adv.* **5**, eaaw3350.
- 1271 Liu M.-C. and Keller L. P. (2017) The beryllium-10 abundance in an unusual hibonite-1272 perovskite refractory inclusion from Allende: Implications for the origin of ¹⁰Be (abstract #1249). *48th LPSC*.
- Liu M.-C., McKeegan K. D., Goswami J. N., Marhas K. K., Sahijpal S., Ireland T. R. and Davis
 A. M. (2009) Isotopic records in CM hibonites: Implications for timescales of mixing of
 isotope reservoirs in the solar nebula. *Geochim. Cosmochim. Acta* 73, 5051–5079.
- 1277 Liu M.-C., Nittler L. R., Alexander C. M. O'D. and Lee T. (2010a) Lithium-beryllium-boron 1278 isotopic compositions in meteoritic hibonite: implications for origin of ¹⁰Be and early 1279 Solar System irradiation. *Astrophys. J.* **719**, L99–L103.
- Lodders K. (2003) Solar System abundances and condensation temperatures of the elements. *Astrophys. J.* **591**, 1220–1247.
- MacPherson G. J. Calcium-aluminum-rich inclusions in chondritic meteorites. In *Meteorites* and Cosmochemical Processes (Ed. A. M. Davis), Vol. 1 Treatise on Geochemistry, 2nd Ed. (Exec. Eds. H. D. Holland and K. K. Turekian), Elsevier, Oxford, pp. 139–179 (2014).
- MacPherson G. J., Kita N. T., Ushikubo T., Bullock E. S., and Davis A. M. (2012) Wellresolved variations in the formation ages for Ca-Al-rich inclusions in the early Solar System. *Earth Planet. Sci. Lett.* **331**, 43–54.

- MacPherson G. J., Bullock E. S., Tenner T. J., Nakashima D., Kita N. T., Ivanova M. A., Krot A. N., Petaev M. I. and Jacobsen S. B. (2017) High precision Al–Mg systematics of forsterite-bearing Type B CAIs from CV3 chondrites. *Geochim. Cosmochim. Acta* **201**, 65–82.
- MacPherson G. J., Huss G. R. and Davis A. M. (2003) Extinct ¹⁰Be in Type A calciumaluminum-rich inclusions from CV chondrites. *Geochim. Cosmochim. Acta* **67**, 3165–3179.
- Makide K., Nagashima K., Krot A. N., Huss G. R., Hutcheon I. D. and Bischoff A. (2009)
 Oxygen- and magnesium-isotope compositions of calcium-aluminum-rich inclusions
 from CR2 carbonaceous chondrites. *Geochim. Cosmochim. Acta* 73, 5018–5050.
- Marhas K. K. and Goswami J. N. (2003) Be-B isotope systematics in CV and CM hibonites: Implications for solar energetic particle production of short-lived nuclides in early Solar System (abstract #1303). *LPSC* **XXIV**.
- Marhas K. K., Goswami J. N. and Davis A. M. (2002) Short-lived nuclides in hibonite grains from Murchison: evidence for solar system evolution. *Science* **298**, 2182–2185.
- McKeegan K. D., Chaussidon M. and Robert F. (2000) Incorporation of short-ived 10Be in a calcium-aluminum-rich inclusion from the Allende meteorite. *Science* **289**, 1334–1337.
- Mendybaev R. A., Richter F. M. and Davis A. M. (2006) Crystallization of melilite from CMAS-liquids and the formation of the melilite mantle of Type B1 CAIs: Experimental simulations. *Geochim. Cosmochim. Acta* **70**, 2622–2642.
- Mendybaev R. A., Williams C. D., Spicuzza M. J., Richter F. M., Valley J. W., Fedkin A. V. and Wadhwa M. (2017) Thermal and chemical evolution in the early solar system as recorded by FUN CAIs: Part II Lab evaporation of potential CMS-1 precursor material. *Geochim. Cosmochim. Acta* **201**, 49–64.
- Mishra R. K. and Chaussidon M. (2015) Timing and extent of Mg and Al isotopic homogenezation in the early inner Solar System. *Earth Planet. Sci. Lett.* **390**, 318–326.
- Mishra R. K. and Marhas K. K. (2019) Meteoritic evidence of a late superflare as source of ⁷Be in the early Solar System. *Nat. Astron.* **4**, 498–505.
- Ogliore R. C., Huss G. R. and Nagashima K. (2011) Ratio estimation in SIMS analysis. *Nucl. Instruments Methods Phys. Res. Sect. B Beam Interact. with Mater. Atoms* **269**, 1910–1918.
- Park C., Nagashima K., Krot A. N., Huss G. R., Davis A. M. and Bizzarro M. (2017) Calciumaluminum-rich inclusions with fractionation and unidentified nuclear effects (FUN CAIs): II. Heterogeneities of magnesium isotopes and ²⁶Al in the early Solar System inferred from in situ high-precision magnesium-isotope measurem. *Geochim. Cosmochim. Acta* **201**, 6–24.
- Park C., Wakaki S., Sakamoto N., Kobayashi S. and Yurimoto H. (2012) Oxygen isotopic composition of the solar nebula gas inferred from high-precision isotope imaging of melilite crystals in an Allende CAI. *Meteorit. Planet. Sci.* **47**, 2070–2083.
- Podosek F. A., Zinner E. K., Macpherson G. J., Lundberg L. L., Brannon J. C. and Fahey A. J. (1991) Correlated study of initial ⁸⁷Sr⁸⁶Sr and AlMg isotopic systematics and petrologic properties in a suite of refractory inclusions from the Allende meteorite. *Geochim. Cosmochim. Acta* **55**, 1083–1110.
- Render J., Ebert S., Burkhardt C., Kleine T. and Brennecka G. A. (2019) Titanium isotopic evidence for a shared genetic heritage of refractory inclusions from different carbonaceous chondrites. *Geochim. Cosmochim. Acta* **254**, 40–53.
- Richter F. M., Mendybaev R. A., and Davis A. M. (2006) Conditions in the protoplanetary disk as seen by type B CAIs. *Meteorit. Planet. Sci* **41**, 83–93.
- Ryerson F. J. and McKeegan K. D. (1994) Determination of oxygen self-diffusion in akermanite, anorthite, diopside, and spinel: Implications for oxygen isotopic anomalies

- and the thermal histories of Ca-Al-rich inclusions. *Geochim. Cosmochim. Acta* **58**, 3713–3734.
- Schrader D. L., Connolly H. C. J., Lauretta D. S., Zega T. J., Davidson J. and Domanik K. J. (2015) The formation and alteration of the Renazzo-like carbonaceous chondrites III: Toward understanding the genesis of ferromagnesian chondrules. *Meteorit. Planet. Sci.* **50**, 15–50.
- Schrader D. L., Franchi I. A., Connolly H. C. J., Greenwood R. C., Lauretta D. S. and Gibson J. M. (2011) The formation and alteration of the Renazzo-like carbonaceous chondrites I: Implications of bulk-oxygen isotopic composition. *Geochim. Cosmochim. Acta* **75**, 308–325.
- Shollenberger Q. R., Borg L. E., Render J., Ebert S., Bischoff A., Russell S. S. and Brennecka G. A. (2018) Isotopic coherence of refractory inclusions from CV and CK meteorites: Evidence from multiple isotope systems. *Geochim. Cosmochim. Acta* 228, 62–80.
- Simon J. I., Ross D. K., Nguyen A. N., Simon S. B. and Messenger S. (2019) Molecular cloud origin for oxygen isotopic heterogeneity recorded by a primordial spinel-rich refractory inclusion. *Astrophys. J.* **884**, L29.
- Simon S. B., Davis A. M. and Grossman L. (1999) Origin of compact type A refractory inclusions from CV3 carbonaceous chondrites. *Geochim. Cosmochim. Acta* **63**, 1233–1248.
- Simon S. B. and Grossman L. (2015) Refractory inclusions in the pristine carbonaceous chondrites DOM 08004 and DOM 08006. *Meteorit. Planet. Sci.* **49**, 1032–1049.
- Simon S. B., Krot A. N. and Nagashima K. (2019a) Oxygen and Al-Mg isotopic compositions of grossite-bearing refractory inclusions from CO3 chondrites. *Meteorit. Planet. Sci.* **54**, 1361 1362–1378.
- Simon S. B., Krot A. N., Nagashima K., Kööp L. and Davis A. M. (2019b) Condensate refractory inclusions from the CO3.00 chondrite Dominion Range 08006: Petrography, mineral chemistry, and isotopic compositions. *Geochim. Cosmochim. Acta* **246**, 109–122.
- Simon S. B., Kuehner S. M., Davis A. M., Grossman L., Johnson M. L. and Burnett D. S. (1994) Experimental studies of trace element partitioning in Ca, Al-rich anorthite and perovskite compositions: *Geochemica Cosmochem. Acta* **58**, 1507–1523.
- Sossi P.A., Moynier F., Chaussidon M., Villeneuve J., Kato C. and Gounelle M. (2017) Early Solar System irradiation quantified by linked vanadium and beryllium isotope variations in meteorites. *Nat. Astron.* **1**, 0055.
- Srinivasan G. and Chaussidon M. (2013) Constraints on ¹⁰Be and ⁴¹Ca distribution in the early solar system from ²⁶Al and ¹⁰Be studies of Efremovka CAIs. *Earth Planet. Sci. Lett.* **374**, 11–23.
- Srinivasan G., Huss G. R. and Wasserburg G. J. (2000) A petrographic, chemical, and isotopic study of calcium-aluminum-rich inclusions and aluminum-rich chondrules from the Axtell (CV3) chondrite. *Meteorit. Planet. Sci.* **35**, 1333–1354.
- Stolper E. and Paque J. M. (1986) Crystallization sequences of Ca-Al-rich inclusions from Allende: The effects of cooling rate and maximum temperature. *Geochim. Cosmochim.* Acta **50**, 1785–1806.
- Sugiura N., Shuzou Y. and Ulyanov A. (2001a) Beryllium-boron and aluminum-magnesium chronology of calcium-aluminum-rich inclusions in CV chondrites. *Meteorit. Planet. Sci.* **1408**, 1397–1408.
- Sugiura N., Shuzou Y. and Ulyanov A. (2001b) Beryllium-boron and aluminum-magnesium chronology of calcium-aluminum-rich inclusions in CV chondrites. **1408**, 1397–1408.
- Tatischeff V., Duprat J. and De Sereville N. (2014) Light-element nucleosynthesis in a molecular cloud interacting with a supernova remnant and the origin of beryllium-10 in the protosolar nebula. *Astrophys. J.* **124**.

- Telus M., Huss G. R., Ogliore R. C., Nagashima K. and Tachibana S. (2013) Recalculation of data for short-lived radionuclide systems using less-biased ratio estimation. *Meteorit*. *Planet. Sci.* **2030**, 2013–2030.
- Thrane K., Nagashima K., Krot A. N. and Bizzarro M. (2008) Discovery of a New FUN CAI from a CV Carbonaceous Chondrite: Evidence for Multistage Thermal Processing in the Protoplanetary Disk. *Astrophys. J.* **680**, L141–L144.
- Torrano Z. A., Brennecka G. A., Williams C. D., Romaniello S. J., Rai V. K., Hines R. R. and Wadhwa M. (2019) Titanium isotope signatures of calcium-aluminum-rich inclusions from CV and CK chondrites: Implications for early Solar System reservoirs and mixing. *Geochim. Cosmochim. Acta* **263**, 13–30.
- Trinquier A., Elliott T., Ulfbeck D., Coath C., Krot A. N. and Bizzarro M. (2009) Origin of nucleosynthetic isotope heterogeneity in the solar protoplanetary disk. *Science* **324**, 374–376.
- Ushikubo T., Tenner T. J., Hiyagon H. and Kita N. (2017) A long duration of the ¹⁶O-rich reservoir in the solar nebula, as recorded in fine-grained refractory inclusions from the least metamorphosed carbonaceous chondrites. *Geochim. Cosmochim. Acta* **201**, 103–1404
- Vacher L. G., Ogliore R. C., Jones C., Liu N. and Fike D. A. (2021) Cosmic symplectite recorded irradiation by nearby massive stars in the solar system's parent molecular cloud. *Geochim. Cosmochim. Acta*.
- 1408 Vermeesch P. (2018) IsoplotR: A free and open toolbox for geochronology. *Geosci. Front.* **9**, 1479–1493.
- Wang J., Davis A. M., Clayton R. N., Mayeda T. K. and Hashimoto A. (2001) Chemical and isotopic fractionation during the evaporation of the FeO-MgO-SiO₂-CaO-Al₂O₃-TiO₂ rare earth element melt system. *Geochim. Cosmochim. Acta* **65**, 479–494.
- Wendt I. and Carl C. (1991) The statistical distribution of the mean squared weighted deviation.

 Chem. Geol. Isot. Geosci. Sect. 86, 275–285.
- Wielandt D., Nagashima K., Krot A. N., Huss G. R., Ivanova M. A. and Bizzarro M. (2012)
 Be in the early Solar System. *Astrophys. J.* 748, L25.
- Williams C. D., Janney P. E., Hines R. R. and Wadhwa M. (2016) Precise titanium isotope compositions of refractory inclusions in the Allende CV3 chondrite by LA-MC-ICPMS. *Chem. Geol.* **436**, 1–10.
- Williams C. D., Ushikubo T., Bullock E. S., Janney P. E., Hines R. R., Kita N. T., Hervig R. L., MacPherson G. J., Mendybaev R. A., Richter F. M. and Wadhwa M. (2017) Thermal and chemical evolution in the early solar system as recorded by FUN CAIs: Part I Petrology, mineral chemistry, and isotopic composition of Allende FUN CAI CMS-1. *Geochim. Cosmochim. Acta* 201, 25–48.
- Yang L. and Ciesla F. J. (2012) The effects of disk building on the distributions of refractory materials in the solar nebula. *Meteorit. Planet. Sci.* **47**, 99–119.
- York D., Evensen N. M., Martínez M. L. and De Basabe Delgado J. (2004) Unified equations for the slope, intercept, and standard errors of the best straight line. *Am. J. Phys.* **72**, 367.
- Yurimoto H., Krot A. N., Choi B.-G., Aleon J., Kunihiro T. and Brearley A. J. (2008) Oxygen Isotopes of Chondritic Components. *Rev. Mineral. Geochemistry* **68**, 141–186.
- Yurimoto H. and Kuramoto K. (2004) Molecular cloud origin for the oxygen isotope heterogeneity in the Solar System. *Science* **305**, 1763–1766.
- Zhai M., Nakamura E., Shaw D. M. and Nakano T. (1996) Boron isotopes in meteorites and lunar rocks. *Geochim Cosmochim Acta* **60**, 4877–4881.

1435 1436